

A High-Frequency Gravitational-Wave Burst Search with LIGO's Hanford Site

by

Jacqueline Rose Villadsen

Submitted to the Department of Physics
in partial fulfillment of the requirements for the degree of

Bachelor of Science in Physics

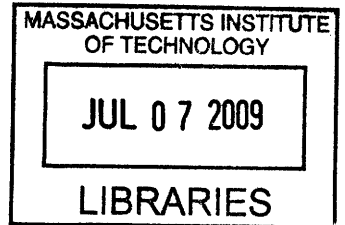
at the

MASSACHUSETTS INSTITUTE OF TECHNOLOGY

June 2009

© Jacqueline Rose Villadsen, MMIX. All rights reserved.

The author hereby grants to MIT permission to reproduce and
distribute publicly paper and electronic copies of this thesis document
in whole or in part.



ARCHIVES

Author

Department of Physics

22 May 2009

Certified by

Erotokritos Katsavounidis

Associate Professor of Physics

Thesis Supervisor

Accepted by

Professor David E. Pritchard

Senior Thesis Coordinator, Department of Physics

A High-Frequency Gravitational-Wave Burst Search with LIGO's Hanford Site

by

Jacqueline Rose Villadsen

Submitted to the Department of Physics
on 22 May 2009, in partial fulfillment of the
requirements for the degree of
Bachelor of Science in Physics

Abstract

The Laser Interferometer Gravitational-Wave Observatory (LIGO) is a network of long-arm interferometers designed to directly measure gravitational-wave strain. Direct observation of gravitational waves would provide a test of general relativity, as well as new insight into high-energy astrophysics. As of yet there have been no confirmed direct observations of gravitational waves, the largest of which are expected to be near the limit of LIGO's sensitivity. Analyses of LIGO data face the challenge of distinguishing small gravitational-wave signals from noise.

This thesis presents a blind analysis of data from LIGO's fifth science run (November 2005-October 2007), searching for high-frequency gravitational-wave bursts coincident in data from the two LIGO interferometers located in Hanford, WA. The search for high-frequency gravitational-wave bursts is motivated by potential astrophysical sources such as supernovae and neutron stars, and enabled by the improvement of LIGO's sensitivity and the extension of the LIGO calibration up to 6 kHz.

This analysis searches for gravitational-wave candidates with a duration under 1 second and central frequency from 1 to 6 kHz, of unspecified signal shape, during times when LIGO's two Hanford detectors were in science mode but its detector in Livingston, LA was not in science mode. The search is a blind analysis, developed using a set of background data that was previously established not to contain any gravitational-wave candidates. The background data are the data from the two Hanford detectors during times when the Livingston detector was in science mode. These background data are used to set requirements for identifying a gravitational-wave candidate in the foreground data, which are the data from the two Hanford detectors when the Livingston detector was not in science mode.

The analysis identifies no gravitational-wave candidates. However, the analysis does set an upper limit on the rate of high-frequency gravitational-wave bursts as a function of signal strength and frequency. The upper limits converge to an upper limit of 0.018 events per day, or 6.5 events per year, at the 90% confidence level, for bursts at or above a characteristic strain amplitude of 10^{-19} strain/ $\sqrt{\text{Hz}}$.

This work does not reflect the scientific opinion of the LIGO Scientific Collaboration and its results have not been reviewed by the collaboration.

Thesis Supervisor: Erotokritos Katsavounidis

Title: Associate Professor of Physics

Acknowledgments

This project benefitted immensely from the efforts of all the scientists and engineers who have designed LIGO and brought it to its current unprecedented level of sensitivity. The LIGO calibration team is basically awesome because they're the reason I have data and not just a jumble of incomprehensible numbers. The LIGO Scientific Collaboration, especially the Burst Analysis Group, came up with the analysis methods used in this project.

I would like to thank my thesis advisor, Professor Erik Katsavounidis, who has been supportive throughout my thesis and willing to make time to read a draft at the very last minute. I also want to thank the members of his research group, especially Lindy Blackburn, who went out of his way more than once to help me.

Out of everyone in the group, I owe the biggest thank you to Dr. Brennan Hughey, who guided me through the whole project and then read the thesis quite a few times too. He also chatted with me when I couldn't stare at a computer screen anymore - an invaluable service.

Last of all, I would like to thank my parents for being wonderful. Also, for paying for my MIT education, because I certainly couldn't have paid for it. And I want to thank everyone at MIT, such as my number one girl Sunita Darbe, for giving me an amazing four years. I have been so happy here and I'm terrified to leave. It cheers me up to think that wherever I go, there will still be physics.

Contents

1	The Theory of Gravitational Waves	9
1.1	Existence of Gravitational Waves	10
1.1.1	Mathematical Description of Gravitational Waves	10
1.1.2	Properties of Gravitational Waves	11
1.2	Sources of Gravitational Waves	13
2	The Search for Gravitational Waves	15
2.1	Indirect Evidence of Gravitational Waves	15
2.2	Direct Detection of Gravitational Waves	16
2.3	The Laser Interferometer Gravitational Wave Observatory	18
2.3.1	Detectors	18
2.3.2	Limitations on a High-Frequency Search	20
2.3.3	Data Analysis	21
2.4	Methods of LIGO's Burst Analysis Working Group	21
2.4.1	QPipeline and Signal Energy	23
2.4.2	CorrPower and the Correlation Statistic Γ	28
3	The Data Set	31
3.1	Description of the Data	31
3.2	Data Quality Flags	33
3.3	Vetoed	36
3.4	Comparison of Year 1 and Year 2	37

4	Design of a Blind Analysis	41
4.1	Outline of Analysis	41
4.2	Parameters of the Analysis	42
4.2.1	Injections	43
4.2.2	The Null Stream Veto	44
4.2.3	The Energy Threshold	45
4.2.4	The Gamma Threshold	45
4.3	Vetoed	46
4.4	Design of Year 1 Analysis	46
4.4.1	Setting the False Alarm Probability	46
4.4.2	Choice of (Z_0, Γ_0) to Maximize Total Efficiency	47
4.4.3	Effect of the Null Stream	48
4.4.4	Coherent vs. Correlated Energy	49
4.4.5	Final Plan for Year 1 Analysis	50
4.5	Design of Year 2 Analysis	51
4.5.1	Setting the False Alarm Probability	52
4.5.2	Optimizing Efficiency	53
4.5.3	Final Plan for Year 2 Analysis	54
4.6	Test of the Analysis on Timelagged Data	54
5	Results and Discussion	59
5.1	Γ Distribution of Triggers	59
5.1.1	Inspection of High- Γ Triggers	60
5.2	Upper Limit Curves	61
5.3	Potential Improvements to the Analysis	63
5.4	Context	65

Chapter 1

The Theory of Gravitational Waves

The search for gravitational waves poses challenges in both instrument design and data analysis. Technological innovations in instrument design are making a global network of gravitational wave detectors more and more sensitive, and yet astrophysical theory predicts that most gravitational waves passing through Earth are of an amplitude still lower than that of the noise in the detectors. The challenge of identifying these signals hidden in the noise makes data analysis a creative and complex task. This project takes on that task for data from the fifth science run of the Laser Interferometer Gravitational Wave Observatory (LIGO). This project searches for gravitational wave bursts in the high-frequency domain, from 1 to 6 kHz, in data from the two LIGO detectors located in Hanford, WA.

Chapter 1 summarizes the theory of the production and propagation of gravitational waves. Chapter 2 discusses the search for gravitational waves, focusing on LIGO's method of detection and data analysis tools. Chapter 3 reviews the quality and characteristics of the high-frequency data from LIGO's fifth science run, which were analyzed in this project. Chapter 4 describes the design of a blind analysis of the data. Chapter 5 presents the results of this analysis.

1.1 Existence of Gravitational Waves

Special relativity provides an intuitive argument for the existence of gravitational waves: If a gravitational field changes over time, for example when two masses are orbiting one another, the information about the change in the gravitational field cannot travel outwards faster than the speed of light. Hence, there will be a ripple in the gravitational field that travels outward no faster than the speed of light - a gravitational wave. The details of the nature of such a wave can be derived from the theory of general relativity.

1.1.1 Mathematical Description of Gravitational Waves

Einstein's theory of general relativity allows a mathematical description of gravitational waves. This section presents a brief overview of that description, following the example of [18]. More detailed derivations are widely available; for example, see [16].

In the mathematical formulation of general relativity, the curvature of spacetime at each point in space and time is determined by a metric $g_{\mu\nu}$, which is a 4×4 matrix, corresponding to the 3 spatial dimensions plus 1 time dimension. The Einstein field equations relate the form of the metric to the energy-momentum tensor $T_{\mu\nu}$, which describes the density of energy and momentum at each point in spacetime. The Einstein field equations can be written:

$$R_{\mu\nu} - \frac{1}{2}Rg_{\mu\nu} = \frac{8\pi G}{c^4}T_{\mu\nu}. \quad (1.1)$$

In Equation 1.1, $R_{\mu\nu}$ is the Ricci curvature tensor, R is the scalar curvature, G is the gravitational constant, and c is the speed of light. The left-hand side of the equation describes the curvature of spacetime, and the right-hand side of the equation describes the energy and momentum at each point in time and space, so the Einstein field equations are the mathematical expression of the statement that matter and energy cause the curvature of spacetime.

In the absence of matter, the simplest solution to the Einstein equations is the

Minkowski metric for special relativity, $g_{\mu\nu} = \eta_{\mu\nu}$.

$$\eta_{\mu\nu} = \begin{bmatrix} -1 & 0 & 0 & 0 \\ 0 & 1 & 0 & 0 \\ 0 & 0 & 1 & 0 \\ 0 & 0 & 0 & 1 \end{bmatrix} \quad (1.2)$$

In the limit of weak fields, a perturbation $h_{\mu\nu}$ is added to this metric in order to satisfy the Einstein equations, so that $g_{\mu\nu} = \eta_{\mu\nu} + h_{\mu\nu}$. There exists a coordinate system, known as the transverse-traceless gauge, in which $h_{\mu\nu}$ has only two independent components:

$$h_{\mu\nu} = \begin{bmatrix} 0 & 0 & 0 & 0 \\ 0 & h_+ & h_\times & 0 \\ 0 & h_\times & -h_+ & 0 \\ 0 & 0 & 0 & 0 \end{bmatrix}. \quad (1.3)$$

With this representation of $h_{\mu\nu}$, the Einstein equations reduce to a simple wave equation:

$$\left(\nabla^2 - \frac{1}{c^2} \frac{\partial^2}{\partial t^2} \right) h_{\mu\nu} = 0. \quad (1.4)$$

1.1.2 Properties of Gravitational Waves

The components h_+ and h_\times in Equation 1.3 are independent of one another, determined by the source of the gravitational wave. They describe two independent polarizations of gravitational waves, known as the “plus” and “cross” polarizations. For a gravitational wave with the plus polarization, the proper interval ds is given by:

$$ds^2 = -c^2 dt^2 + (1 + h_+) dx^2 + (1 - h_+) dy^2 + dz^2. \quad (1.5)$$

Consider a bar oriented in the x-direction with proper length L . Using the fact that h_+ is a small perturbation, the change in length of the bar turns out to be:

$$\frac{\Delta L}{L} = -\frac{h_+}{2}. \quad (1.6)$$

This equation shows that the amplitude h of a gravitational wave is directly proportional to the fractional change in length scales caused by that wave. h is measured in the dimensionless unit of strain, where one unit of strain corresponds to $\Delta L/L = 1$. LIGO is designed to measure strains on the scale of 10^{-21} at frequencies near 100 Hz [8].

A gravitational wave propagating in the z -direction causes space to be compressed and stretched along the transverse axes - compressed in one direction, and stretched in the perpendicular direction. As the wave propagates, the amplitude of the stretching and compressing oscillates over time between $1 + |h_+|/2$ and $1 - |h_+|/2$. For the cross polarization, the effect is similar, except that the stretching and compressing occurs at an orientation of 45° with respect to the plus polarization. Figure 1-1 shows the effect on a ring of matter as waves of the two polarizations pass through it.

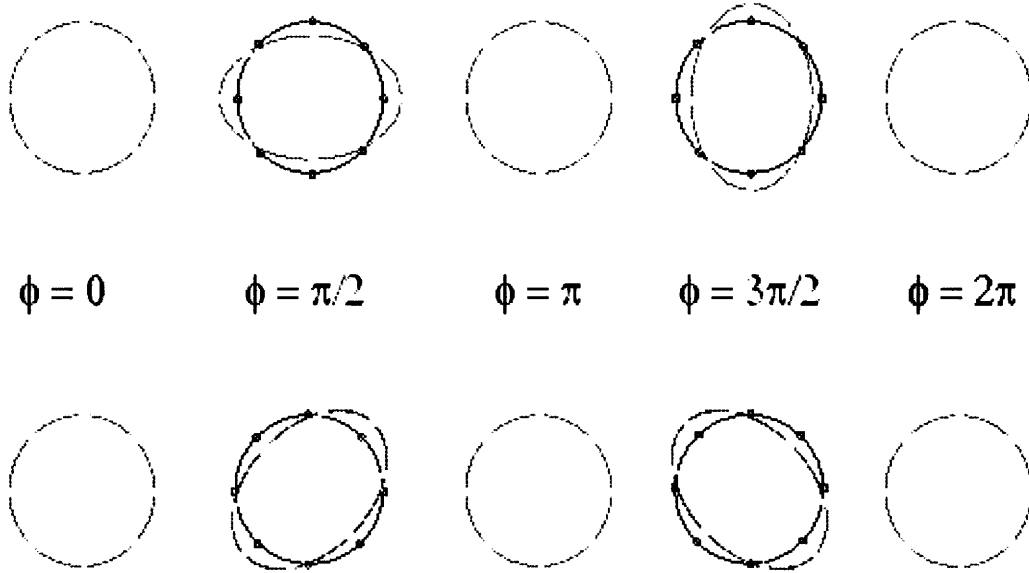


Figure 1-1: Each row shows the effect on a circular ring of matter as a gravitational wave passes through it. The top row shows the effect of a plus-polarized wave; the bottom, the effect of a cross-polarized wave. The series of images represent snapshots taken at different times during the period of the wave; the phase of the wave in each image is indicated by ϕ . Figure from [15].

As a gravitational wave propagates outwards over time, it retains its initial form. Gravitational waves interact only weakly with matter, so matter does not have a

damping effect on gravitational waves. A gravitational wave decreases in energy flux as the inverse square of the distance r from the source, as its energy spreads out over a sphere of greater and greater radius, just as the flux of light decreases as the inverse square of the distance from the source. Photodetectors measure the intensity of light, which is proportional to $1/r^2$ like the energy flux. By contrast, gravitational-wave interferometers measure the amplitude of the gravitational wave, which goes as $1/r$. As a consequence, compared to electromagnetic observations, small improvements in the sensitivity of gravitational-wave detectors open up a large volume of space to observation.

1.2 Sources of Gravitational Waves

In order for a mass distribution to produce gravitational radiation, it must change in an asymmetrical way. The special-relativity explanation of gravitational waves provides a simple explanation for this: if a gravitational field changes but remains spherically symmetric, for example if a star collapses symmetrically, because of Gauss's Law the field will remain constant outside the original radius of the mass in question, so no ripple will travel outwards through the gravitational field. More formally, the requirement for a mass distribution to produce gravitational radiation is that the second time derivative of at least one of its multipole moments must be non-zero [40]. The mass monopole moment is conserved because of conservation of energy. The mass dipole moment is conserved because of conservation of momentum. The next multipole moment is the quadrupole moment. A system with a non-zero second derivative of the quadrupole moment of the mass distribution will produce gravitational radiation.

The gravitational waves most likely to be detectable on Earth should arise from processes involving the flux of high amounts of matter and energy. A laboratory experiment to produce gravitational waves might consist of a rotating dumbbell with two large masses on either end; if the masses weighed 1 ton each with a separation of 2 m and a rotational frequency of 1 kHz, the gravitational radiation produced would still only have a strain of approximately 10^{-38} [34], which is more than 10 orders of

magnitude lower than a number of predicted signals from astrophysical sources.

This project consists of a search for short gravitational-wave bursts in the high-frequency range, from about 1 kHz to 6 kHz. There are a number of possible astrophysical sources of gravitational radiation in this frequency domain. Supernova collapses are in some cases predicted to generate gravitational waves with high-frequency components [32]. A number of processes involving neutron stars may also produce gravitational radiation in these frequencies: neutron stars collapsing into rotating black holes [10, 11]; mergers between two neutron stars with a stiff equation of state, briefly forming a hypermassive neutron star [31]; normal modes of oscillation in neutron stars [35]; and the precession of a neutron star due to accretion from a binary companion [25]. High-frequency gravitational waves may also be associated with gamma-ray flares from soft gamma repeaters [22]. High-frequency gravitational waves could also probe into fundamental particle physics; particle theorists have proposed high-frequency GW sources including mergers of lunar-mass primordial black holes [24], and cosmic string cusps [29].

Chapter 2

The Search for Gravitational Waves

This chapter briefly summarizes methods of gravitational wave detection, then focuses on the long-arm interferometers of the Laser Interferometer Gravitational Wave Observatory (LIGO). It concludes in an overview of the untemplated burst search methods used by the LIGO Burst Analysis Group, in particular QPipeline, which was used by this project.

2.1 Indirect Evidence of Gravitational Waves

Although there have been no widely-accepted direct detections of gravitational waves, considerable indirect evidence supports their existence. Hulse and Taylor [23] received the Nobel Prize in Physics for their 1974 discovery of the first known pulsar in a binary system, PSR 1913+16. General relativity predicts that the system should lose energy to gravitational radiation. Observation of the system over the years since its discovery has shown that the orbit is decaying at a rate within 0.3% of the general relativistic prediction [43], providing strong support for the theory of gravitational radiation. In addition, three other binary pulsars have since been discovered that also agree with the prediction for energy loss due to gravitational radiation [13, 33, 37].

2.2 Direct Detection of Gravitational Waves

Two primary methods have been used for direct detection of gravitational waves. The first generation of gravitational-wave detectors were resonant mass detectors, pioneered by Joseph Weber in the 1960s [42]. Resonant mass detectors generally consist of large aluminum cylinders. When a gravitational wave passes through a resonant mass detector, it changes the dimensions of the cylinder. If the wave has a frequency component near the resonant frequency of the cylinder, it will excite resonant vibrations. Detectors measure the amplitude of vibrations and hence the amplitude of the gravitational wave strain.

Laser interferometers were first proposed by Gertsenshtein and Pustovoit [21] in 1962 as an alternative method of direct detection of gravitational waves. Robert Forward, a student of Joseph Weber, constructed the first operating interferometer [30]. In 1972, Rainer Weiss [44] published independent work on the subject that has led to the gravitational-wave interferometers operating today. Figure 2-1 shows the basic design of a laser interferometer. An interferometer has an “L” shape, whose two perpendicular arms are, at minimum, hundreds of meters in length. At the corner of the L, a beam splitter is used to split laser light into both arms of the L. Each arm has a mirror at both ends, so that light is stored between the mirrors and travels the length of the arm many times before recombining with light from the other arm. The recombined beam has an interference pattern that changes if the length of the arm changes. Since gravitational waves stretch space in one direction perpendicular to their direction of propagation, and compress space in the other transverse direction, the length of the arms will be most affected by gravitational waves coming from directly overhead the detector, as shown in Figure 2-1. Thus, laser interferometers are most sensitive to gravitational radiation traveling perpendicular to the plane of the detector, polarized in alignment with the arms of the interferometer.

A number of laser interferometer gravitational wave detectors around the world have contributed to the search for gravitational waves. These include the 2-km detector and two 4-km detectors in the United States, belonging to LIGO [27]; GEO600, a

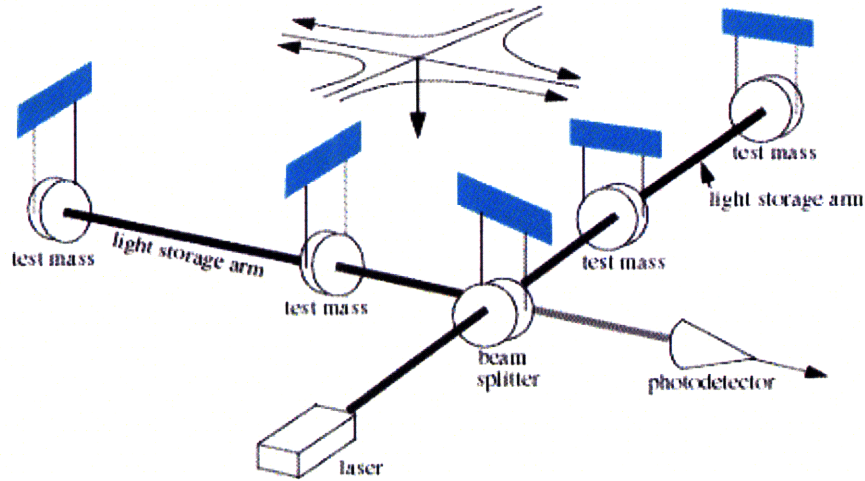


Figure 2-1: Schematic of a laser interferometer gravitational wave detector. A gravitational wave is shown above the detector, moving downwards. The arrows show the direction of gravitational-wave strain: the wave stretches space along one axis and compresses it in the other. Depending on the orientation of an incident gravitational wave, it will change the length of the detector's arms differently, changing the interference pattern detected by the photodetector. Figure from [28].

600-m detector in Germany [20]; TAMA, a 300-m detector in Japan [39]; and Virgo, a 3-km detector in Italy [41]. Collaboration between the detectors allows searches for signals that are coincident in all the detectors, which increases the signal-to-noise ratio of any true gravitational waves. Furthermore, since standard general relativity predicts that gravitational waves travel at the speed of light, the difference in arrival time at different detectors can be used to reconstruct the direction on the sky from which a gravitational wave originates. The data analysis presented in this thesis, however, only considers data from LIGO. LIGO's detectors were the most sensitive detectors in data-collection mode during the times covered by this analysis, so including other detectors would not significantly increase the sensitivity of the search.

2.3 The Laser Interferometer Gravitational Wave Observatory

The Laser Interferometer Gravitational Wave Observatory consists of a network of three detectors. Two of the detectors, one with 4-km arms and one with 2-km arms, are located in Hanford, WA; the third detector, with 4-km arms, is located in Livingston, LA. LIGO has been in operation since 2001 and has been in data-collection mode, known as “science mode,” for only a fraction of the time since then. In the intermediate time, engineering improvements gradually brought LIGO to its design sensitivity. Until 2005, the longest science run had only lasted about two months. LIGO’s fifth science run (S5) started in November 2005, and lasted two years to October 2007; LIGO attained its design sensitivity partway through the first year of S5. These two factors - the length of the data run and the attainment of design sensitivity - have allowed an unprecedented sensitivity in the search for gravitational waves.

2.3.1 Detectors

This section gives a brief overview of the LIGO detectors, drawing on a review of LIGO written during the fifth science run [1], which provides a more detailed description of the apparatus.

The LIGO detectors have been very precisely engineered to reduce noise levels. Each of the detectors is located in a high vacuum of less than 10^{-8} torr in order to prevent sound waves and light scattering off of gas particles. The two Hanford detectors share the same vacuum chamber. The beam source is a 10-W, 1064-nm Nd:YAG laser with frequency stabilization, modulated with a radio frequency signal. The optics in the interferometers are isolated using a system of pendulums and springs, which strongly attenuate environmental vibrations, especially at high frequencies.

A feedback loop uses servo motors to minutely adjust the length of the interferometer arms in order to keep optical power at a minimum at a port of the photodetector. The control signals from this feedback loop reflect the changes in the interference pat-

tern of the recombined laser light from the two arms of the interferometer. The digital output of these control signals is converted to the gravitational-wave strain $s(t)$ by a non-linear response function. The response function is determined by controlled experiments in which the servo motors are used to move the mirrors minutely and the change in the interference pattern - and hence the change in arm length - is measured.

LIGO data also include many auxiliary channels that provide information about operating conditions. There are auxiliary channels monitoring the conditions of most components of the interferometer, such as the variation of laser power and frequency. Auxiliary channels also include environmental information such as data taken by seismometers on site at each of the interferometers. The readouts from auxiliary channels are used for two purposes: first, to characterize the noise sources; second, to create data quality flags and vetoes that indicate when the main channel data should be rejected because of unusual behavior in one of the auxiliary channels, such as a surge in laser power.

The sensitivity of the LIGO detectors is generally given by an amplitude spectral noise density, in units of $\text{strain}/\sqrt{\text{Hz}}$, which is the square root of the noise power spectral density. Figure 2-2 shows the sensitivity curves for H1, H2, and L1 from early in the fifth science run. For frequencies above 200 Hz the primary noise source is shot noise. Shot noise is due to the statistical fluctuations in the number of photons counted, which becomes important at high frequencies because the shorter period means that fewer photons can be counted per period. At high frequencies, noise peaks appearing in narrow frequency bands are generally due to vibrational modes of some element of the interferometer, in particular the wires that suspend the mirrors at each end of the arms, and to power line harmonics at frequencies that are multiples of 60 Hz.

The sensitivity curves in Figure 2-2 show only the noise floor. Another measure of noise in LIGO data is its glitchiness. Glitches are short bursts in the $s(t)$ data that may resemble gravitational-wave signals, but are not actually from gravitational waves. LIGO data analysis faces the challenge of distinguishing true gravitational-wave signals from glitches.

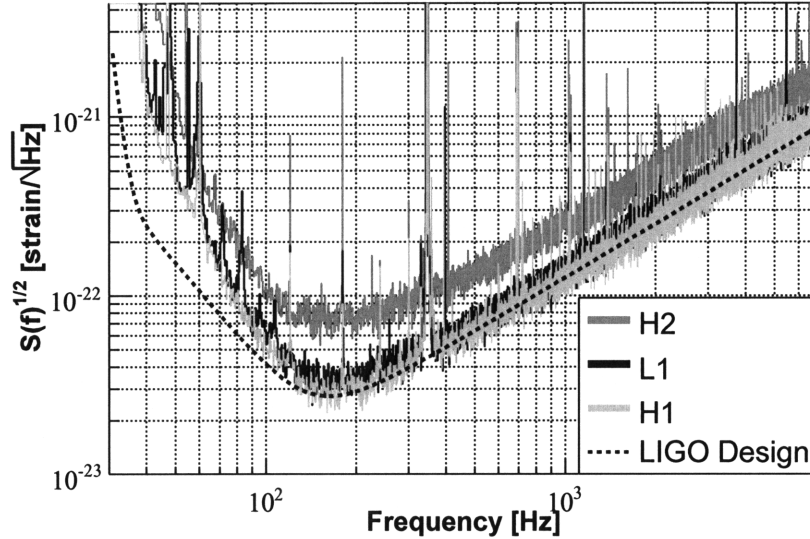


Figure 2-2: Sensitivity curve from the beginning of LIGO's fifth science run. By February 2006, significant improvements had been made to the sensitivity of the detectors. Figure from [7].

2.3.2 Limitations on a High-Frequency Search

The highest frequency detectable by LIGO is its Nyquist frequency of 8192 Hz, since LIGO has a sampling frequency of 16384 Hz. However, LIGO is most sensitive around 200 Hz, and most analyses of LIGO data have not extended above 2 kHz. Furthermore, the calibration of LIGO data only extends to about 6 kHz.

Still, there are many interesting signals that may be detected in the high-frequency range (see Section 1.2), which the lower-frequency analyses might not detect. Hence, an analysis of the LIGO data in the high-frequency domain complements the lower-frequency analyses, maximizing the amount of information learned from the LIGO data.

A high-frequency analysis is constrained by different noise sources than a low-frequency analysis. In Figure 2-2, the low-frequency side of the sensitivity curve arises from a number of different noise sources such as seismic disturbances and thermal vibration of the components of the detector. A high-frequency burst search avoids these noise sources, and is primarily limited by shot noise. At high frequencies, shot

noise is proportional to frequency. The amplitude uncertainty of each interferometer is limited by shot noise at high frequencies. This uncertainty is on the order of 10% at frequencies from 1 to 6 kHz. Amplitude uncertainty is the primary source of error in this analysis.

2.3.3 Data Analysis

The LIGO Scientific Collaboration has a number of data analysis groups, focused on different aspects of the search for gravitational waves. The Compact Binary Coalescence group conducts templated searches for the gravitational-wave signature of the inspiral and merger of a compact binary system [6]; the signal should increase in frequency and amplitude as the system approaches the merger. The Continuous Wave Working Group seeks to identify continuous, periodic gravitational-wave signals in the LIGO data [4], which would most likely originate from pulsars. The Stochastic Sources Upper Limit Group develops upper limits on the amplitude of a universal gravitational-wave background [3], which may originate from the early universe, like the Cosmic Microwave Background, or may originate from numerous unresolved astrophysical sources. The Burst Analysis Working Group searches for short bursts - of much less than a second in duration - of unspecified origin at all frequencies of the LIGO data [2]. This thesis was conducted in the Burst Analysis Group, which is described in greater detail below.

2.4 Methods of LIGO's Burst Analysis Working Group

LIGO's Burst Analysis Working Group has searched for gravitational-wave bursts in the S5 data in both the low- and high-frequency regimes. The search includes both triggered searches, which seek to identify a gravitational-wave burst corresponding to an astrophysical event, and all-sky searches, which search for gravitational-wave bursts from anywhere in the sky at any time for which data are available. The all-sky

burst search over low frequencies, from 64 Hz to 2000 Hz, for the first year of S5, is described in [5]. The all-sky high-frequency burst search for the first year of S5 [7] examined data from 1 kHz to 6 kHz from all three LIGO interferometers. This thesis contributed to the high-frequency search, considering data only from the H1 and H2 interferometers during times when L1 was not in science mode, and extended the analysis through the second year of S5, beyond the scope of [7]. During the second year of S5, Virgo started operating in science mode, so the Burst Analysis Group of the LIGO-Virgo Collaboration is currently working on an analysis of the data from the second year of S5; the paper describing this analysis is not yet available.

The Burst Analysis Group’s data analysis pipelines follow a basic formula:

1. Data quality flags are applied to a set of “background” data (data known not to contain gravitational-wave signals; see Section 3.1), removing time segments when an auxiliary channel indicates the detector was not performing well.
2. A search algorithm identifies instants in time, called “triggers,” with significant signal energy and cross-correlation between detectors.
3. Additional data quality cuts and vetoes (see Section 3.3) are applied, cutting out individual triggers.
4. The remaining triggers are plotted as the background distribution, which is used to set a significance threshold for considering a trigger a gravitational-wave candidate.
5. Hardware or software injections of mock gravitational-wave signals are added to background data and analyzed to determine the sensitivity of the search.
6. Steps 1-3 are repeated to analyze the foreground data, and any triggers which pass the significance threshold are considered to be gravitational-wave candidates.

This section describes the different search algorithms used in Step 2; the overall pipeline will be discussed more thoroughly in Chapter 4.

The search algorithms all follow a certain pattern:

1. The strain data $s(t)$ is decomposed onto the time-frequency plane.
2. Time-frequency tiles containing a significant excess of power [9] are identified as triggers.
3. Each trigger is checked for consistency between H1, H2, and L1 in time and signal shape.

The low-frequency S5 year 1 analysis used three independent data analysis pipelines, each one with a different search algorithm. One of the algorithms, QPipeline [17,18], divides up the time-frequency plane into tiles of constant area, and identifies excess power separately in L1 and in a signal H_+ that combines H1 and H2; the program CorrPower may be used to determine the correlation between the detectors. CorrPower was not used with QPipeline in the low-frequency search, but it was used in the high-frequency search [7].

In the low-frequency analysis, the three search algorithms performed equally well to within a factor of two at all frequencies [5]. The high-frequency S5 year 1 analysis chose to use only the third search algorithm, combining the analysis tools QPipeline and CorrPower. Following the high-frequency analysis, this thesis uses the combination of QPipeline and CorrPower to search for high-frequency bursts in the data from H1 and H2.

2.4.1 QPipeline and Signal Energy

QPipeline is an analysis tool that analyzes the LIGO timestream data $s(t)$ in overlapping blocks of 16 seconds. For each block, QPipeline maps $s(t)$ onto the time-frequency plane, using the Q transform, and creates a list of triggers that have excess power in one or more time-frequency tiles.

Data Whitening

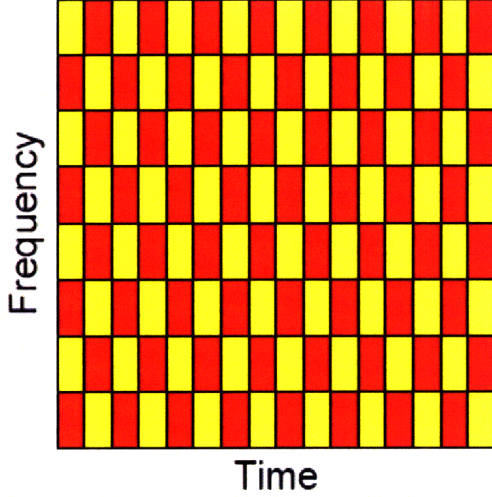
Before applying the Q transform to LIGO data, QPipeline uses zero-phase linear predictive filtering [18] to whiten the data. White noise is noise that has a flat power spectral density, meaning that each frequency of noise has the same amplitude. LIGO noise is not originally white noise, as can be seen in Figure 2-2. Data whitening is the process of renormalizing the noise by frequency so that it has a flat spectral density. A gravitational-wave signal should not be removed by the filtering because the filtering is applied to a much longer time scale than the duration of the gravitational wave.

The Q Transform

One way to analyze the frequency content of the gravitational-wave strain signal is to divide up the LIGO livetime into short, equal lengths of time, and run a Fourier transform on the data from each block of time to analyze the frequency content of that block of time individually. Applying the Fourier transform like this maps a time-domain signal onto the time-frequency plane with tiles of constant duration and bandwidth, as shown in Figure 2-3. However, the length of time necessary to detect a high-frequency signal is much shorter than to detect a low-frequency signal; so choosing to tile the time-frequency plane with blocks of equal time duration at each frequency would sacrifice either the ability to resolve the precise time at which a high-frequency signal occurred, or the ability to detect low-frequency signals.

The Q transform [17, 18] is similar to the discrete short-time Fourier transform, which maps a time-domain signal onto sinusoids, resulting in a representation of the time-frequency plane with tiles of constant shape. By comparison, the Q transform maps a time-domain signal onto a set of windowed sinusoids with a constant quality factor Q (approximately the number of cycles in the waveform), resulting in a representation of the time-frequency plane with tiles of varying shape. The QPipeline algorithm in particular first applies a Fourier transform to $h(t)$, changing it to the frequency-domain $\tilde{h}(f)$, then maps it onto bisquare-windowed complex exponentials in the frequency domain. Figure 2-3 shows the tiling of the time-frequency plane using

Short Time Fourier Transform



Discrete Constant Q-Transform

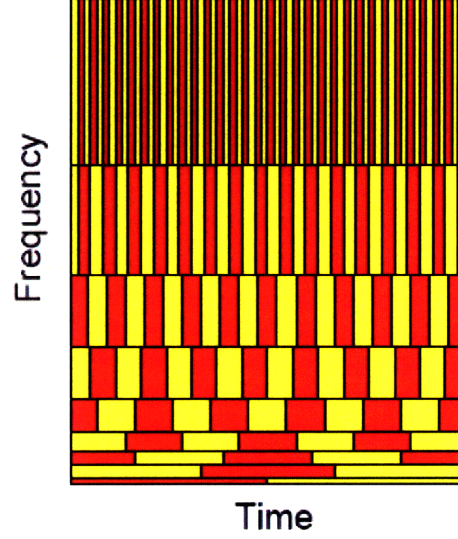


Figure 2-3: The Fourier transform and the Q transform map timestream data onto the time-frequency plane with different tiling schemes. The Fourier transform uses tiles of constant duration and bandwidth, whereas the Q transform uses tiles of shorter duration for higher frequency. Figure from [36].

the Q transform. The tiles all have constant area, but their duration and bandwidth vary. Since the tiles are of longer duration for low frequencies, it is possible to detect lower-frequency signals without sacrificing the ability to resolve the time at which high-frequency bursts occur. QPipeline actually maps the burst onto a number of versions of the time-frequency plane, tiled using different values of Q . When a burst is represented with this tiling scheme, the tile with the largest signal energy should contain at least 80% of the total signal energy [18], so a single tile can be used to represent a burst without much loss of signal energy. The Q transform is thus a useful tool for a burst search, making it flexible for detecting signals of different frequencies.

The equation for the Q transform is:

$$X(\tau, f_0, Q) = \int_{-\infty}^{+\infty} \tilde{x}(f) \tilde{w}(f, f_0, Q) e^{+i2\pi f\tau} df, \quad (2.1)$$

where

$$\tilde{w}(f, f_0, Q) = \left(\frac{315}{128\sqrt{5.5}} \frac{Q}{f_0} \right)^{1/2} \left[1 - \left(\frac{fQ}{f_0\sqrt{5.5}} \right)^2 \right]^2 \quad (2.2)$$

is the function for the bisquare window, normalized to unity. The bisquare window is additionally defined to be zero for frequencies greater than $f_0\sqrt{(5.5)}/Q$. The bisquare window is an approximation to a Gaussian window that maximizes the efficiency of the QPipeline search.

Normalized Energy

When the square of the Q transform coefficient, $|X(\tau, f_0, Q)|^2$, is averaged over many tiles with different values of τ at the same frequency f_0 , it gives an approximate value for the square of the noise spectral density at that frequency. Averaging over all tiles, varying both τ and f_0 , measures the noise level due to all frequencies. The normalized energy Z in a single tile is defined as

$$Z(\tau, f_0, Q) = \frac{|X(\tau, f_0, Q)|^2}{\langle |X(\tau, f_0, Q)|^2 \rangle}. \quad (2.3)$$

The normalized energy is a measure of the signal energy in a tile relative to the level of noise. It is related to the signal-to-noise ratio ρ :

$$\hat{\rho}^2 = Z - 1. \quad (2.4)$$

The Coherent Stream H_+ and The Null Stream H_-

Since the two Hanford detectors, H1 and H2, are located at the same location, with the same orientation, gravitational waves should appear at the same time in both signals with the same form and the same strain. QPipeline adds the two signals to obtain a coherent data stream H_+ , and applies the Q transform to H_+ in order to obtain the “coherent energy” Z^{Coh} .

The coherent stream is the noise-weighted sum of the data streams from H1 and

H2. The frequency representation is calculated as follows:

$$\tilde{s}_{H_+}(f) = \left(\frac{1}{S_{H1}} + \frac{1}{S_{H2}} \right)^{-1} \left(\frac{\tilde{s}_{H1}(f)}{S_{H1}} + \frac{\tilde{s}_{H2}(f)}{S_{H2}} \right), \quad (2.5)$$

where $\tilde{s}_{H1}(f)$ and $\tilde{s}_{H2}(f)$ are the data streams from H1 and H2 in the frequency domain, and S_{H1} and S_{H2} are their power spectral densities.

The null stream H_- is calculated in the same manner as Equation 2.5, but subtracting rather than adding the contribution from H2, to obtain the noise-weighted difference of H1 and H2.

Coherent and Correlated Energy

The coherent energy Z^{Coh} is calculated as described in Equation 2.3, but using the coherent stream H_+ rather than the data stream from one of the individual interferometers. If Equation 2.5 for the coherent stream is plugged into Equation 2.3 to obtain the coherent energy, it turns out that the coherent energy contains terms related to the coherent energy of the individual streams, and a cross-term related to the correlation between the two streams. The terms determined by the coherent energy of the individual streams are combined as:

$$|X^{inc}|^2 = \left(\frac{1}{S_{H1}} + \frac{1}{S_{H2}} \right)^{-2} \left(\frac{|X_{H1}|^2}{S_{H1}^2} + \frac{|X_{H2}|^2}{S_{H2}^2} \right), \quad (2.6)$$

where X_{H1} and X_{H2} are the Q transforms of the data from the two interferometers as defined by Equation 2.1. $|X^{inc}|$ is then used to calculate the normalized incoherent energy:

$$Z^{inc} = \frac{|X^{inc}|^2}{\langle |X^{inc}|^2 \rangle}. \quad (2.7)$$

The correlated energy Z^{Corr} is the difference between the coherent and incoherent energies, so that only the cross-terms remain, describing the correlation of the data streams from the two interferometers. The correlated energy is calculated as:

$$Z^{corr} = Z^{coh} - Z^{inc}. \quad (2.8)$$

2.4.2 CorrPower and the Correlation Statistic Γ

After triggers have been identified using QPipeline, they may be further analyzed using CorrPower [14]. CorrPower is an analysis program that compares the shape of the trigger's strain data across multiple interferometers and produces a correlation statistic Γ . CorrPower may be applied to H1, H2, and L1 in a triple-coincident analysis; in this analysis it was only applied to H1 and H2.

Given the GPS time of a trigger, CorrPower first calculates Pearson's linear correlation statistic r between the whitened time stream data from two different interferometers. r is the dot product of data vectors representing the two time streams, normalized to their magnitude, calculated as follows:

$$r = \frac{\sum_{i=1}^N (s_{H1}(t_i) - \overline{s_{H1}}) (s_{H2}(t_i) - \overline{s_{H2}})}{\sqrt{\sum_{i=1}^N (s_{H1}(t_i) - \overline{s_{H1}})^2} \sqrt{\sum_{i=1}^N (s_{H2}(t_i) - \overline{s_{H2}})^2}}, \quad (2.9)$$

where N is the number of samples in the integration window, and $\overline{s_{H1}}$ and $\overline{s_{H2}}$ are the mean values of $s_{H1}(t)$ and $s_{H2}(t)$ within the integration window.

The r -statistic can be used to calculate the probability that the two data sequences are uncorrelated. The cross-correlation statistic G is defined as the absolute value of the base-10 logarithm of the probability that the two sequences are uncorrelated. Thus, G can have any positive value, and a greater G value indicates a stronger cross-correlation.

The cross-correlation is calculated for a range of different central times, and a range of integration windows from 10 to 50 ms, yielding many values for G . The Γ statistic is defined as the maximum value of G .

CorrPower is insensitive to a potential phase shift between the detectors because in addition to varying central time and integration window, the program time shifts the H1 signal relative to the H2 signal by increments up to a maximum time shift of 1 ms. The program calculates the Γ statistic for each time shift, and returns the highest Γ value from all the time shifts.

The Γ statistic is useful for ruling out coincident false alarms, whose signal shape

should not be correlated between different detectors. A true gravitational wave should produce the same shape signal, with differences due only to detector noise, in all LIGO interferometers since they are approximately co-aligned and thus all have the same sensitivity to the two gravitational-wave polarizations.

Chapter 3

The Data Set

3.1 Description of the Data

In general, gravitational wave searches with LIGO are performed as blind analyses, meaning that the method for identifying a gravitational-wave candidate is decided upon before examining the foreground data. “Foreground data” refers to the data in which the analysis searches for gravitational waves. The foreground data in this analysis are the data from the Hanford detectors, H1 and H2, during times when the Livingston detector (L1) was not operational during LIGO’s fifth science run (S5). S5 lasted two years, from November 2005 to October 2007.

In order to design the analysis without using the foreground data, the analysis is trained on another data set known as the background data. The background data should have the same characteristics as the foreground data, such as noise level, but should be known to contain no detectable gravitational waves.

A true gravitational wave should appear in all of LIGO’s detectors, whereas noise ideally should not be correlated between the detectors. Shifting the data from one interferometer by a time interval, relative to the data from another interferometer, creates an artificial data set. This data set is known as a “time slide,” and should have the same level of noise and random coincidence of glitches between the detectors. Time slides do not contain any true gravitational waves because the minimum time shift used is required to be much greater than the light travel time between the

LIGO detectors. Hence, time slides fulfill the requirements for the background data set and are often used as such. Analyses generally use at least one hundred different time slides to create a background data set about one hundred times larger than the foreground.

This analysis, however, did not use time slides to tune the analysis. The analysis only uses data from H1 and H2, the two detectors located in Hanford. These detectors may have correlated noise due to their geographic proximity, which is less of a problem in triple-coincident analyses since the Livingston detector is much farther away. Data quality cuts, based on the auxiliary channels, should remove most of these disturbances, but this is still a potential problem. Using time slides for the background would ignore any correlated noise, possibly resulting in a too-low estimation of the noise level.

Instead of time slides, the background for this analysis consists of the data from LIGO's two-year-long fifth science run (S5) when all three interferometers were operational. These data have already been analyzed in a high-frequency triple-coincident burst searches using QPipeline, which did not detect any gravitational waves. That analysis is more sensitive than this double-coincident analysis, so for the purposes of this analysis the data it analyzed can be considered not to contain any gravitational waves. Additionally, the times when L1 was on or off should have no correlation to the noise levels of the Hanford detectors, so this data set should have the same noise level as the foreground. Thus, the data from when all three interferometers were operational can be used as the background once it has been established that they contain no gravitational waves. This background, unlike time slides, is limited to the length of time when all three detectors were on. For year 1 of S5, the background is 158.7 days, about twice the length of the foreground of 76.6 days. For year 2 of S5, the background is 193.3 days, almost four times the length of the foreground of 53.5 days.

Table 3.1: Data Quality Flags

Category	Percentage of Livetime Removed	
	Year 1	Year 2
Category 1	1.1%	0.8%
Category 2	0.3%	0.2%
Category 3	0.6%	0.3%

3.2 Data Quality Flags

Data quality (DQ) flags are defined by the LIGO Detector Characterization group to indicate times when the LIGO data may be of low quality. Some DQ flags are defined as the data are acquired, and others are defined later by examination of the auxiliary channels. The goal of DQ flags is to remove a high percentage of non-gravitational-wave triggers without removing a high percentage of the livetime.

There are four categories of DQ flags, which vary in terms of severity. Category 1 flags list times when the data should not be processed by search algorithms, including when the detector is not in science mode and when the data are corrupted. Category 2 flags indicate data which should not be examined for detection candidates, because of a malfunction in the detector that has a proven correlation to the gravitational-wave strain channel; flags are removed after running QPipeline because they divide the data up into many short time segments, and QPipeline runs better on fewer long segments. Category 3 flags mark times that should not be included when setting an upper limit on gravitational-wave events if the analysis finds no gravitational-wave candidates (see Section 5.2), but a trigger during these times may still be investigated as a gravitational-wave candidate. Category 4 flags do not reject data from the analysis, but suggest caution in examining the affected data; they come from sources such as local events recorded in the LIGO logs by operators.

This analysis follows the S5 year 1 high-frequency triple-coincident search [7] in applying only a select group of the category 3 flags, since many of the category 3 flags

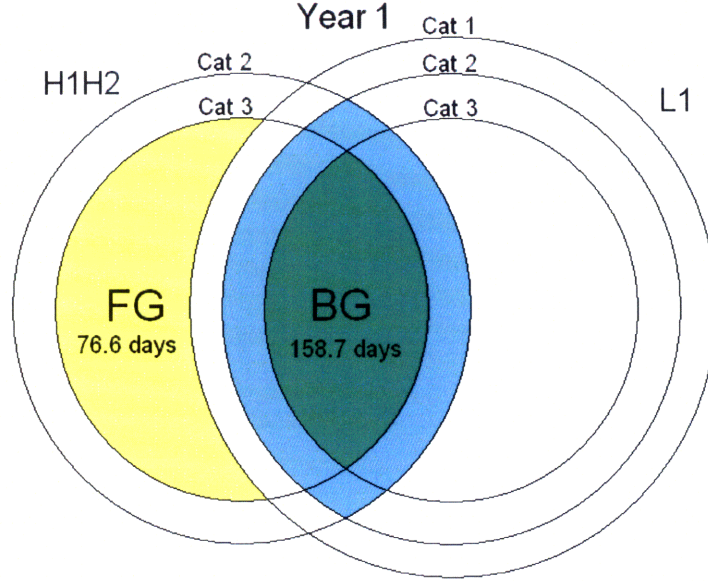


Figure 3-1: Year 1 data set. “Cat 1” to “Cat 3” refer to data that have passed the different levels of data quality cuts. H1H2 refers to times when the data from both Hanford detectors were available; L1 refers to the Livingston detector. The S5 year 1 triple-coincident high-frequency burst search [7] analyzed the region in blue, and found no gravitational-wave candidates, so it could be used as background (the green region) for this search. The yellow region indicates the foreground of this search, which had not been analyzed before.

primarily affect the low-frequency data. The year 1 triple-coincident search applied only the category 3 flags for which the rate of high-frequency triggers was at least 1.7 times higher when the flag was on compared to when the flag was off. The same method was later used to determine the relevant category 3 flags for year 2. The category 3 flags that were applied are shown in Table 3.2.

The triple-coincident analyses at low and high frequencies for year 1 of S5 both search for gravitational-wave candidates during the times flagged by category 3. Because this analysis only checks for double coincidence rather than the more rigorous standard of triple coincidence, it was decided to ensure data quality by removing the category 3 flags at the same time as category 2, without searching for gravitational-wave candidates in the category 3 flags. As indicated in Table 3.1, this did not result in a large loss of livetime.

Figures 3-1 and 3-2 show the data used for the background and foreground in years

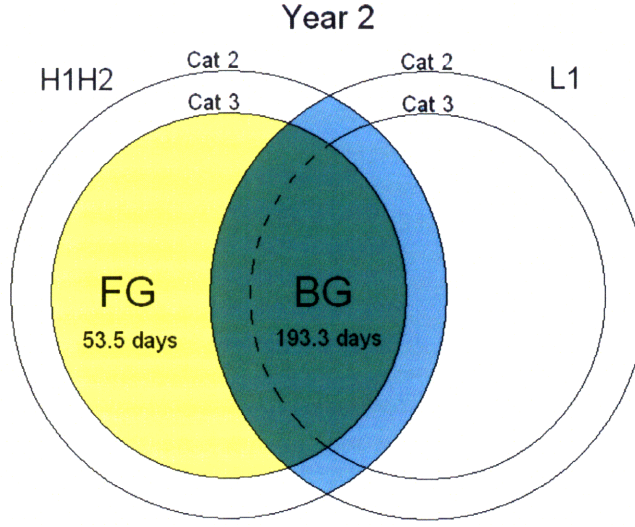


Figure 3-2: Year 2 data set. An informal S5 year 2 triple-coincident high-frequency burst search analyzed the region in blue, and found no gravitational-wave candidates, so it could be used as background (the green region) for this search. The yellow region indicates the foreground of this search, which had not been analyzed before.

1 and 2, respectively. The triple-coincident high-frequency burst search, which determined that the background contained no gravitational-wave candidates, analyzed all data that passed the category 2 DQ cuts. The analysis presented by this thesis only used the part of the data that had passed category 3 cuts relevant to H1 and H2. This analysis of the year 2 data analyzes all available, relevant data. In contrast, the year 1 analysis excludes from the background the H1H2 cat 3 data that did not pass the L1 cat 3 cuts; from the foreground it excludes the H1H2 cat 3 data that did not pass the L1 cat 1 cuts. This exclusion occurred because the background and foreground were analyzed separately with QPipeline for year 1, and including those data would have resulted in many short segments, which are difficult to process with QPipeline. This exclusion resulted in a 2% reduction of the year 1 livetime. In the year 2 analysis this problem was resolved by running QPipeline on the background and foreground data together, and then splitting up the data afterwards.

Table 3.2: Category 3 DQ Flags

Year	Name	Explanation
Both years	H1:LIGHTDIP_02_PERCENT	Significant dip in laser light power stored in H1
Year 1 only	H2:LIGHTDIP_04_PERCENT	Significant dip in laser light power stored in H2
	H1:SIDECOIL_ETMX_RMS_6HZ	Saturation of side coil current in H1 end mirror
	H1:WIND_OVER_30MPH	High wind speeds around H1 arms
	H1:DARM_09_11_DHZ_HIGHTHRESH	Up-conversion of seismic noise at 0.9 to 1.1 Hz
Year 2 only	H1:DARM_11_13_DHZ_LOWTHRESH	Up-conversion of seismic noise at 1.1 to 1.3 Hz
	H1:DARM_18_24_DHZ_LOWTHRESH	Up-conversion of seismic noise at 1.8 to 2.4 Hz

3.3 Vetoes

In addition to data quality cuts, vetoes are also used to remove $s(t)$ data that shows correlation to auxiliary channels. Vetoes remove much shorter time segments than data quality cuts - generally on the order of 100 ms - and they are determined on a purely statistical basis. An automatic, hierarchical veto generation system was used to generate vetoes for the year 1 high-frequency burst search [7]. These vetoes were also used in this analysis. The same system was also used to create vetoes for the analysis of year 2.

The veto generation system, described in [7], compares many of the auxiliary channels to the main channel. The veto generation system was applied to a background created by timeslides of L1 relative to H1H2. If a short transient, on the order of 1 ms, in an auxiliary channel is correlated to a heightened rate of background triggers in the gravitational-wave strain channel within approximately 100 ms, a veto is created that cuts out short segments of time whenever a large enough transient occurs in that

auxiliary channel. Rather than applying all possible vetoes, the potential vetoes are ranked according to their efficiency-to-deadtime ratios. This ratio is calculated as the percentage of background triggers removed by the veto, divided by the percentage of the livetime lost by applying the veto. After the most effective veto is selected, the efficiency-to-deadtime ratios of the other vetoes are recalculated, and then the second most effective veto is selected. This process is repeated until all remaining potential vetoes have an efficiency-to-deadtime ratio of less than 3, or a Poisson probability of their effect occurring randomly of greater than 10^{-5} . For year 1, as reported in [7], the vetoes removed 12% of the triggers from the time-shifted background used for the veto training, at a cost of only 2% of the livetime of the analysis.

3.4 Comparison of Year 1 and Year 2

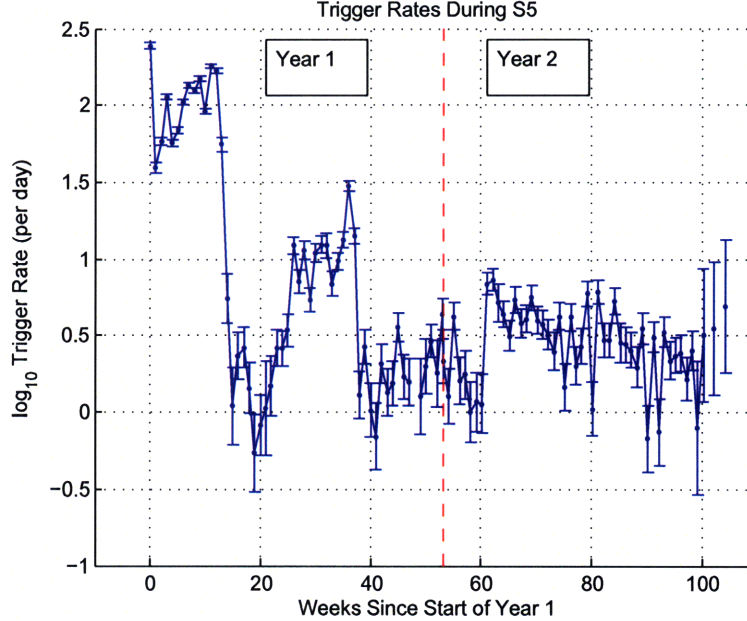


Figure 3-3: Trigger rates during LIGO’s fifth science run. The figure only includes triggers with coherent energy $Z^{Coh} \geq 30$ that have passed the data quality cuts. The dashed red line indicates the transition between year 1 and year 2. Bin size is one week. The trigger rate was highest during the early part of year 1. After 4 months, the trigger rate was reduced by more than one order of magnitude, due to improvements made to the detectors.

Figure 3-3 shows the trigger rate per day, averaged over each week, for the two years of LIGO's fifth science run. The plot only shows triggers with a coherent energy greater than or equal to 30, that have passed the data quality cuts since only these triggers were considered in this analysis. The trigger rate was calculated by dividing the number of triggers in each week by the total livetime during that week. Improvements made to the detectors during the first few months of year 1 resulted in a reduction of the trigger rate by more than one order of magnitude.

Due to improvements made to L1 in year 1, L1 operated in science mode for a larger fraction of year 2, so the year 2 triple-coincident livetime was longer than for year 1. This allowed a slightly better estimation of the background distribution in year 2.

Figure 3-4 shows the right tails of the Z distributions of triggers from the year 1 and year 2 backgrounds, normalized to livetime. As expected, the overall year 2 trigger rate is somewhat lower than for year 1 due to the improvements made to LIGO during the first few months of year 1. In addition to lowering the noise floor, these improvements lowered the rate of glitches, resulting in the lower trigger rate.

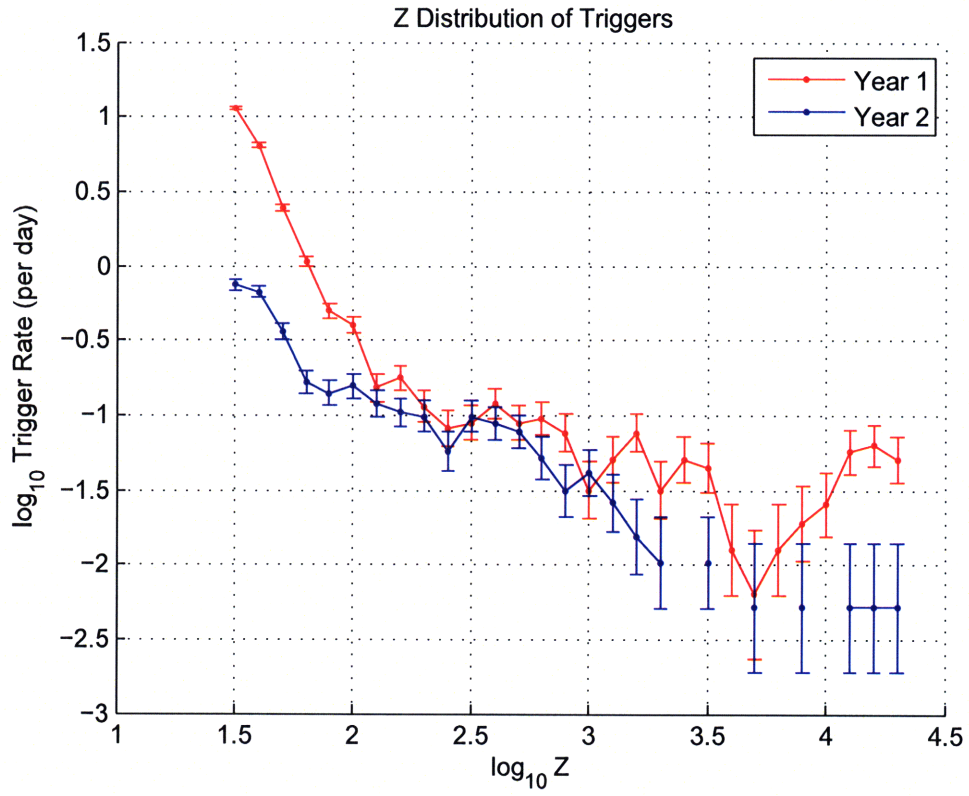


Figure 3-4: The coherent energy distributions of year 1 and year 2 background triggers that have passed the data quality cuts. The distributions are expressed as a rate, triggers per day, which is the total number of triggers during that year, divided by the livetime from that year.

Chapter 4

Design of a Blind Analysis

To tune the analysis, the background data are analyzed using QPipeline and CorrPower, the same analysis tools that will be used on the foreground data. Using the results from QPipeline and CorrPower, thresholds are chosen for the normalized energy Z and cross-correlation statistic Γ . If any triggers in the foreground data pass these thresholds, they will be considered gravitational-wave candidates.

The Z and Γ thresholds are chosen to create a certain probability of a false alarm. The false alarm probability (FAP) is the probability of a foreground trigger passing both thresholds if the foreground only contains noise. This analysis is tuned for a conservative false alarm probability of 1 in 100. This means that, given many data sets of noise with no gravitational waves, with the same time duration as the foreground and the same noise distribution as the background, this analysis would falsely detect a gravitational-wave candidate in 1 in 100 of the data sets.

4.1 Outline of Analysis

The analysis of the foreground data will consist of running the data through two pipelines, then applying data quality cuts and vetoes, selecting only triggers that pass both the Z and Γ thresholds. The steps of this analysis are:

1. Apply Category 1 data quality cuts to data.

Table 4.1: Summary of Options for Analysis

(a) Z^{Coh} -based cut H_- veto not applied	(b) Z^{Corr} -based cut H_- veto not applied
(c) Z^{Coh} -based cut H_- veto applied	(d) Z^{Corr} -based cut H_- veto applied

2. Run QPipeline - may or may not apply null stream veto.
3. Apply Category 2 and 3 data quality cuts to data.
4. Apply vetoes to data.
5. Select for triggers that pass the Z threshold.
6. Run CorrPower.
7. Any triggers that pass the Γ threshold are gravitational-wave candidates.

4.2 Parameters of the Analysis

Requiring a false alarm probability of 1 in 100 places only one requirement on the Z and Γ thresholds, which means that there is a (Z, Γ) curve along which all points provide this false alarm probability, from which a single pair of (Z, Γ) thresholds must be chosen for the final analysis. Other decisions must also be made: whether or not to apply the null stream veto when running QPipeline, and whether the normalized energy threshold should be based on coherent energy (Z^{Coh}) or correlated energy (Z^{Corr}); these options are summarized in Table 4.1. All of these decisions can be made based on a single principle: maximizing the efficiency of detection of gravitational waves.

4.2.1 Injections

In order to measure the efficiency of detection of gravitational waves, software injections of varying amplitude and frequency are added randomly throughout the background data, using the software BurstMDC and GravEn [38]. The background data with injections are then re-analyzed with QPipeline and CorrPower, and the number of injections which pass each (Z, Γ) threshold is counted. The parameters for the analysis will be chosen to maximize the number of injections detected, which corresponds to the efficiency of detection of gravitational waves. These parameters will be used to analyze the foreground data.

The software injections are all Gaussian-enveloped sine waves with quality factor $Q=9$. The equation for such a wave is:

$$h(t_0 + t) = h_0 \sin(2\pi f_0 t) \exp\left(-\frac{(2\pi f_0 t)^2}{2Q^2}\right). \quad (4.1)$$

The amplitude h_0 , central frequency f_0 , and central time t_0 were varied over: fifteen different amplitudes from $h_{rss} = 1.5 \times 10^{-21}$ to $h_{rss} = 1.8 \times 10^{-19}$ strain/ $\sqrt{\text{Hz}}$; three frequencies, 2000 Hz, 3067 Hz, and 5000 Hz; and approximately 1000 different central times for each amplitude and frequency of injection, spaced randomly throughout the background data set such that no injections overlapped. h_{rss} is the amplitude of the gravitational wave, integrated over time:

$$h_{rss} = \sqrt{\int (|h_+(t)|^2 + |h_\times(t)|^2) dt}. \quad (4.2)$$

h_{rss} has units of strain/ $\sqrt{\text{Hz}}$.

In the design of this analysis, two types of injections are used: injections with the same amplitude and phase in H1 and H2, referred to as “non-phase-shifted” injections; and injections with a 50% percent amplitude difference and a phase shift, dependent on frequency, between H1 and H2, referred to as “phase-shifted” injections. The phase-shifted injections were used to evaluate the effects on this analysis of the amplitude and phase uncertainty of the LIGO calibration. At most frequencies, the

Table 4.2: Amplitude and Phase Offset of Phase-Shifted Injections

Frequency	Amplitude Ratio	Phase Offset
2000 Hz	1.5:1	44°
3067 Hz	1.5:1	67°
5000 Hz	1.5:1	110°

actual amplitude and phase uncertainty is much lower than that used for the set of phase-shifted injections, but the minimum phase difference of injections was limited by the sampling rate of 16384 Hz, since injections could not be offset relative to one another by less than one sample, or approximately 60 microseconds. Table 4.2 shows the phase and amplitude difference for each of the three frequencies of phase-shifted injections. By comparison, the LIGO calibration at the time of the analysis predicted phase shifts of 10° to 20° in the high-frequency range.

The injections with phase and amplitude differences reveal that certain choices for the analysis are particularly sensitive to phase and amplitude offset, so these choices will be avoided in order to preserve sensitivity of the analysis in the high-frequency range. However, since the phase-shifted injections overestimate the phase shifts, the injections that are identical in H1 and H2 will ultimately be used to determine the efficiency of detection of the analysis.

4.2.2 The Null Stream Veto

The null stream (H_-) veto, applied by QPipeline, removes triggers for which the difference between the amplitudes in H1 and H2 is greater than a certain fraction of the overall amplitude of the trigger (see Section 2.4.1 for a more detailed explanation). In the design of the year 1 analysis, QPipeline was run twice on the background data and the injections: once without applying the null stream veto, and once applying the null stream veto with an uncertainty factor of 0.1. The uncertainty factor is a measure of the amount of difference permitted between H1 and H2 relative to the overall amplitude of the trigger.

4.2.3 The Energy Threshold

The energy threshold of the analysis could be based on either the coherent energy Z^{Coh} or the correlated energy Z^{Corr} . The coherent energy is a measure of the total combined energy in H1 and H2, whereas the correlated energy measures only the energy of the part of the signal that is correlated between H1 and H2 (see Section 2.4.1 for a more in-depth explanation). The advantage of a cut based on the correlated energy is that it should, on average, be zero, unless the signals in H1 and H2 are truly correlated, so any triggers that pass the cut should already show some correlation between H1 and H2. This aspect of the correlated energy cut is somewhat redundant, since CorrPower fulfills the same purpose of checking the correlation between H1 and H2. A large phase shift between the detectors at high frequencies could result in a low value for correlated energy, even for large gravitational waves; coherent energy, on the other hand, should not be as sensitive to phase shifts. However, the coherent energy may be large when there is a large signal in one detector and essentially no signal in the other. Both coherent and correlated energy have potential benefits for use as an energy threshold; the decision of which one to use will be based on which one maximizes the efficiency of detection of the software injections.

4.2.4 The Gamma Threshold

Requiring a false alarm probability of 1/100 in the analysis of the foreground data results in a fixed relationship between the energy threshold and the Γ threshold. For a range of values for the energy threshold (Z^{Coh} = 30 to 150 with step size 1, and Z^{Corr} = 10 to 22 with step size 0.1), a Γ threshold was chosen to fix the FAP at 1/100. To do so, for each energy threshold the Γ distribution of triggers that passed that cut was plotted and then an exponential curve was fit to the right tail of the distribution using the Levenberg-Marquardt method to minimize χ^2 :

$$n = Ae^{-b\Gamma}. \quad (4.3)$$

From the exponential fit, a Γ threshold was determined that set the FAP at 1/100:

$$\Gamma_0 = \frac{1}{b}[\ln(\frac{A}{b}) - \ln(\delta) - \ln(FAP) + \ln(\frac{t_{fg}}{t_{bg}})]. \quad (4.4)$$

In this equation, A and b come from Equation 4.3, δ is the size of the bins in the histogram to which the exponential fit was applied, and t_{fg}/t_{bg} is the ratio of the foreground livetime to the background livetime.

Applying Equation 4.4 to the exponential fit for each energy cut provides a set of many (Z, Γ) pairs that all achieve a false alarm probability of 1/100. The (Z, Γ) threshold that maximizes the efficiency of detection of injections will be used in the final analysis.

4.3 Vetoes

Due to a small oversight, the analyses for both years were designed without applying vetoes to the background data. Fortunately, this error changed the analysis in the conservative direction. Later, to estimate the effect of this error, vetoes were applied to the background, and eliminated about half the triggers. Failure to apply the vetoes resulted in a higher value of Γ_0 than necessary for a false alarm probability of 1/100, effectively decreasing the false alarm probability by a factor of 2. Failure to apply the vetoes did not affect the outcome of the analysis, described in Chapter 5. If a gravitational-wave candidate were detected by the analysis, vetoes would have been applied.

4.4 Design of Year 1 Analysis

4.4.1 Setting the False Alarm Probability

The FAP was fixed at 1/100 as described in Section 4.2.4. Figure 4-1 shows the Γ distribution of triggers that passed a threshold of $Z_0^{Coh} = 100$. Similar plots were created for values of Z_0^{Coh} from 30 to 150 with step size 1, and Z_0^{Coh} from 10.0 to

18.0 with step size 0.1.

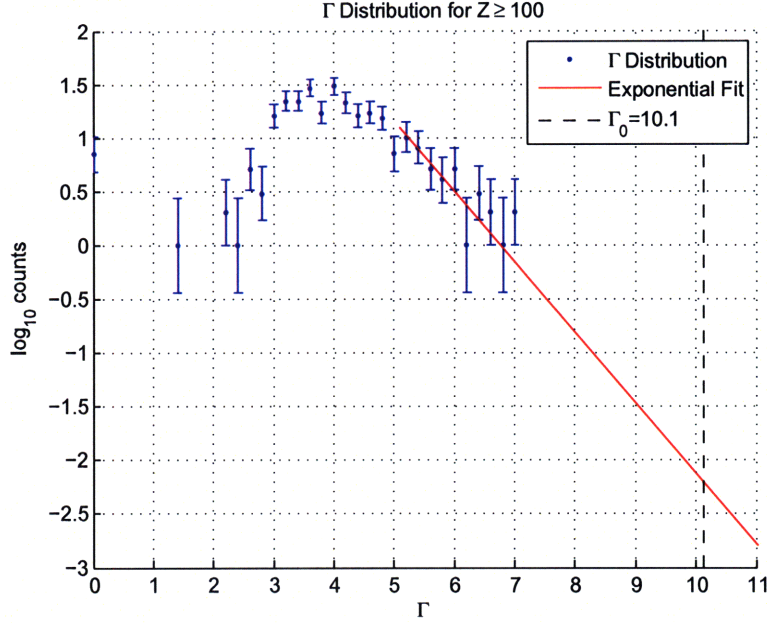


Figure 4-1: Γ distributions of triggers that passed a threshold of $Z_0^{Coh} = 100$. The red line shows the exponential fit to the histogram, and the dotted black line indicates the value for Γ_0 chosen to create a false alarm probability of 1/100. The exponential fit had $\chi^2_{dof} = 0.7$ with 9 degrees of freedom.

Figure 4-2 shows the relationship between Z_0^{Coh} and Γ_0 . The non-smoothness of the curve is an artificial effect due to the limited number of triggers in the background distribution. As the value of Z_0^{Coh} increases, the number of triggers that pass the Z cut may remain constant, and so Γ_0 remains constant. When another trigger is eliminated, the value of Γ_0 jumps.

4.4.2 Choice of (Z_0, Γ_0) to Maximize Total Efficiency

The background data with injections added were analyzed, and then for each possible (Z_0, Γ_0) pair, the number of triggers (due to all types of injections) that passed both the thresholds were counted, and divided by the total number of injections to yield the “total efficiency” for that (Z_0, Γ_0) pair. Figure 4-3 shows Z_0^{Coh} versus the total efficiency. Values of Z_0^{Coh} and Z_0^{Corr} that maximized the total efficiency were chosen.

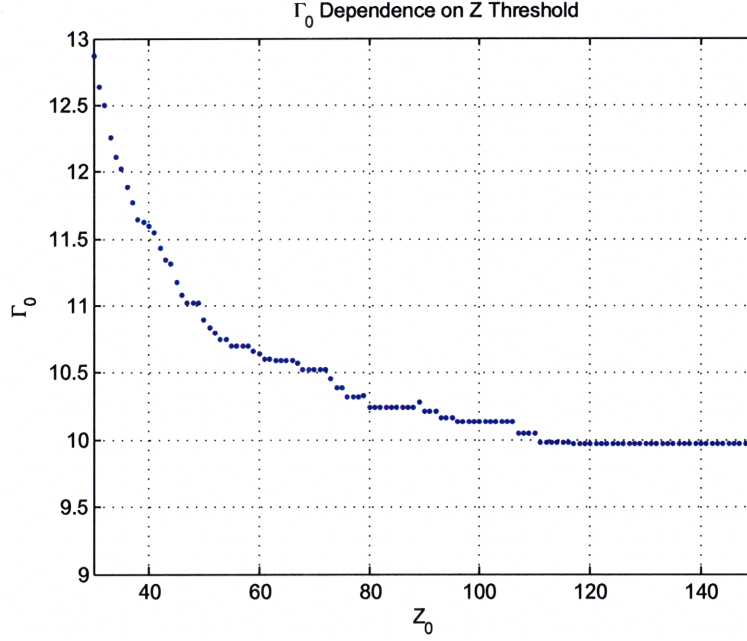


Figure 4-2: The dependence of the Γ threshold on the Z_0^{Coh} threshold for year 1. The relationship between Γ_0 and Z_0^{Coh} is determined by setting a false alarm probability of $1/100$. The curve is not smooth because there are multiple values of Z_0^{Coh} that yield the same background distribution, since there are a limited number of background triggers, and hence these values of Z_0^{Coh} are also assigned the same Γ_0 .

These values are given in Table 4.3.

4.4.3 Effect of the Null Stream

The background data were analyzed with and without the null stream veto applied during QPipeline. In the case when the null stream veto was applied, the steps above were followed to find (Z, Γ) thresholds. However, another option for the analysis existed. When the null stream veto was not applied, a few triggers had values of up to $Z=20,000$, but the null stream veto cut out these high- Z triggers, making it possible to set a Z threshold that would create a false alarm probability of $1/100$ without applying a Γ threshold at all. This turned out to be more efficient than using a combination of a Z threshold and a Γ threshold. Table 4.3 shows the Z thresholds that created a false alarm probability of $1/100$ when the null stream veto was applied, in addition to the (Z, Γ) when it was not applied.

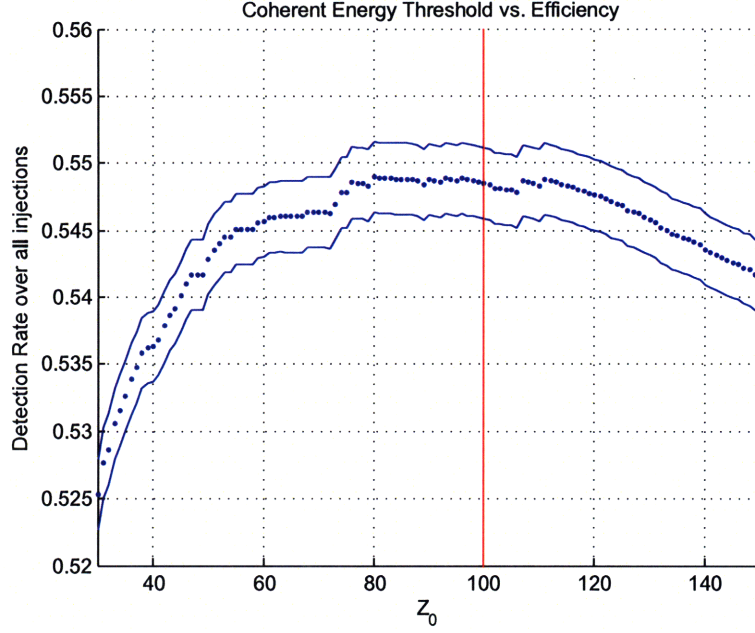


Figure 4-3: The efficiency of detection of all types of injections in year 1 background data for a range of Z_0^{Coh} thresholds. The blue lines indicate the errors on the total efficiency. The red line marks $Z_0^{Coh} = 100$, which would be at the maximum efficiency if the efficiency curve was smooth.

With the non-phase-shifted injections, applying the null stream veto yielded a modest improvement in efficiency. However, the null stream veto is extremely sensitive to phase shifts between H1 and H2. At the time of the analysis the S5 calibration had not been finalized, but at high frequencies the phase uncertainty was predicted to be up to about 20 degrees. An informal study conducted for the triple-coincident high-frequency search determined that such a phase shift between H1 and H2 would result in very low efficiencies of detection, so it was decided not to apply the null stream veto. An added benefit of this decision is that it is in keeping with the triple-coincident high-frequency analysis.

4.4.4 Coherent vs. Correlated Energy

To decide whether to cut based on coherent or correlated energy, the efficiency of detection for each frequency and amplitude of injections was compared. Figure 4-4 shows the result of this comparison for the injections with amplitude and phase

Table 4.3: (Z_0, Γ_0) to Maximize Efficiency

(a) $Z_0^{Coh} = 100$ $\Gamma_0 = 10.1$	(b) $Z_0^{Corr} = 14$ $\Gamma_0 = 10.4$
(c) null stream veto $Z_0^{Coh} = 90$	(d) null stream veto $Z_0^{Corr} = 21$

shifts. Because of the larger phase shifts included at higher frequencies, the coherent energy-based cut is more efficient at 5000 Hz, and the two are essentially equivalent at lower frequencies. The comparison of efficiency for the injections with no phase or amplitude difference is not shown, because for these injections the two types of cuts yield the same efficiencies.

Based on these efficiencies, the conclusion was to use a Z^{Coh} threshold, rather than a Z^{Corr} threshold, because the coherent energy threshold is equivalent with non-phase-shifted injections and more efficient with phase-shifted injections. Additionally, the decision to cut based on coherent energy agrees with the triple-coincident high-frequency analysis.

4.4.5 Final Plan for Year 1 Analysis

The analysis of the year 1 foreground data was finalized as:

1. Run QPipeline (do not apply null stream veto)
2. Apply Z threshold: $Z \geq 100$
3. Apply data quality cuts
4. Run CorrPower
5. Apply Γ threshold: $\Gamma \geq 10.1$

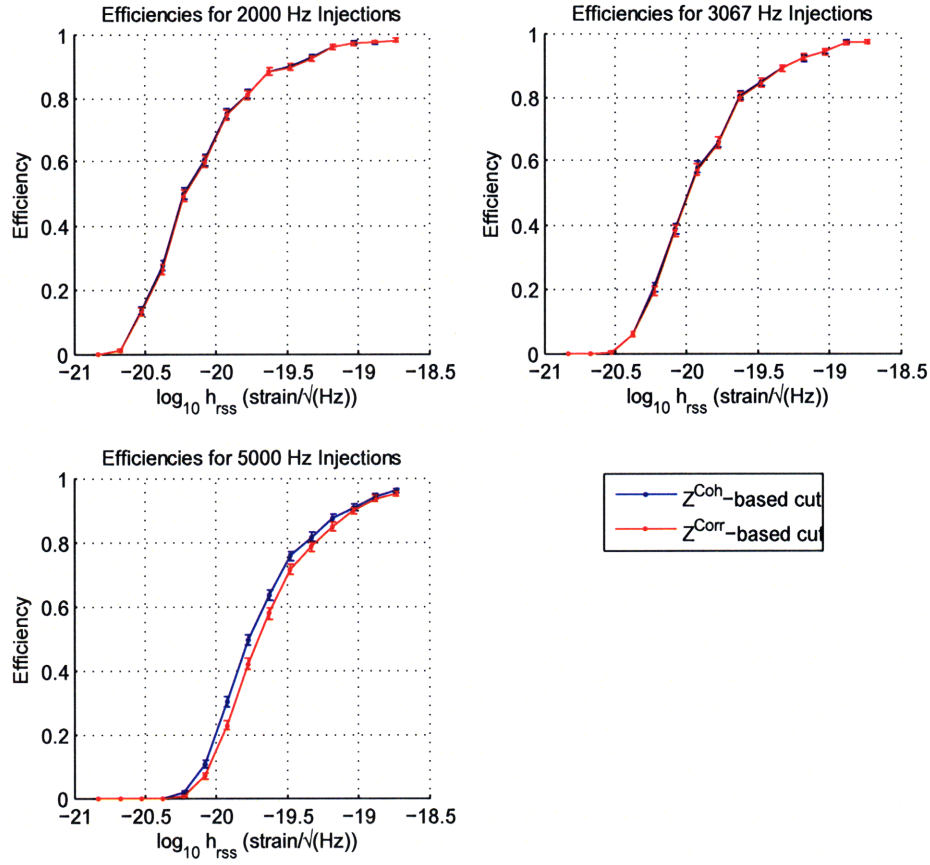


Figure 4-4: The efficiency of detection of phase-shifted injections in year 1 background data using normalized energy cuts based on Z^{Coh} and on Z^{Corr} . The cuts based on Z^{Coh} are slightly more efficient for the highest frequency of injections, 5000 Hz, and the two are almost equivalent at lower frequencies. The errors on the efficiencies come from the binomial statistics of the number of injections detected.

6. Apply vetoes

This analysis plan yields an efficiency of detection of sine-Gaussian injections (with no phase or amplitude shift) as shown in Figure 4-5.

4.5 Design of Year 2 Analysis

The division between year 1 and year 2 was a circumstantial decision that did not reflect fundamental qualities of the data. Hence, the decisions from the year 1 analysis

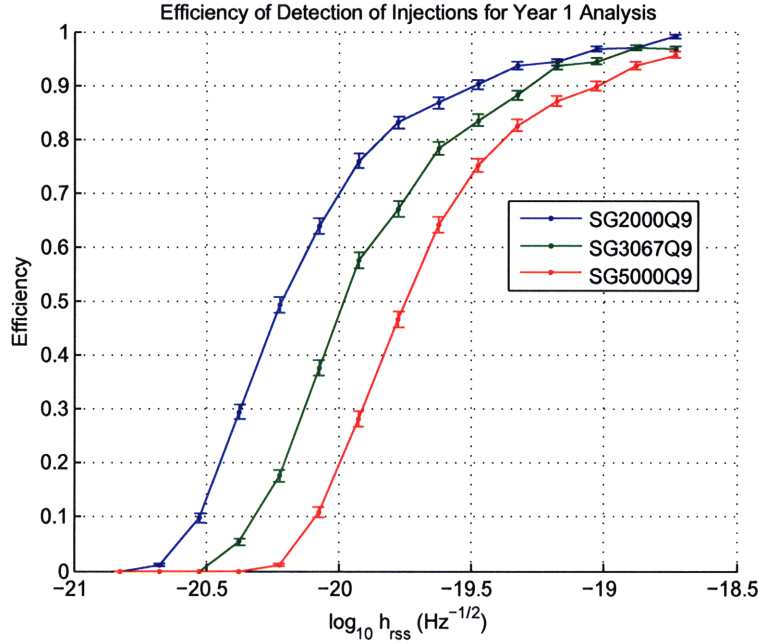


Figure 4-5: The efficiency of detection of injections, with no amplitude or phase shift, in year 1 background data, according to the final thresholds chosen for the year 1 analysis: $Z_0^{\text{Coh}} = 100$ and $\Gamma_0 = 10.1$.

not to apply the null stream veto, and to cut based on coherent rather than correlated energy, should have a similar effect on efficiencies for year 2 as for year 1, so these decisions were applied to year 2 without reexamination. This simplified the design of the analysis for year 2. For year 2, it was only necessary to determine the $(Z_0^{\text{Coh}}, \Gamma_0)$ pair that maximized the efficiency of detection of injections. To do so, non-phase-shifted injections were used.

4.5.1 Setting the False Alarm Probability

Figure 4-6 shows the Γ distribution of triggers from the year 2 background that passed a threshold of $Z_0^{\text{Coh}} = 75$. As for year 1, exponential fits were made to the Γ distributions for Z^{Coh} thresholds ranging from 30 to 150 with step size 1.

Figure 4-7 shows the relationship between the Z^{Coh} and Γ thresholds in order to create a false alarm probability of 1/100. Compared to Figure 4-2, the analogous figure from the year 1 analysis, the Z vs. Γ curve appears jumpy. This because the

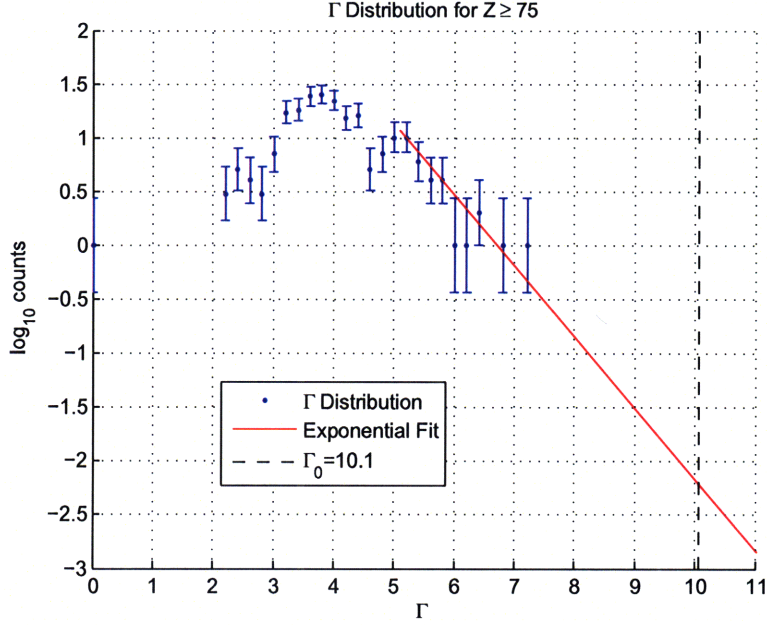


Figure 4-6: Γ distribution of triggers from year 2 background that passed a threshold of $Z_0^{Coh} = 75$. The red line shows the exponential fit to the histogram, and the dotted black line indicates the value for Γ_0 chosen to create a false alarm probability of $1/100$. The exponential fit had $\chi_{dof}^2 = 0.5$ with 10 degrees of freedom. The low χ_{dof}^2 may be attributed to the fact that the Poisson error $\sqrt{(n)}$ on the number of counts n is only an approximation when n approaches zero.

exponential fit is based only on triggers with $\Gamma \geq 5.2$. The second year is less noisy so in the range of Z shown there are considerably fewer triggers with $\Gamma \geq 5.2$, which means that the Z vs. Γ curve has fewer, larger jumps as the triggers are eliminated one by one by the increasing Z threshold.

4.5.2 Optimizing Efficiency

Figure 4-8 shows the total efficiency of detection of injections for the range of Z^{Coh} thresholds considered. A coherent energy threshold of $Z_0^{Coh} = 75$ maximized the efficiency, which corresponded to $\Gamma_0 = 10.1$. The coherent energy threshold is lower for year 2 than for year 1, suggesting that the improvements made to LIGO during year 1 may have reduced glitchiness.

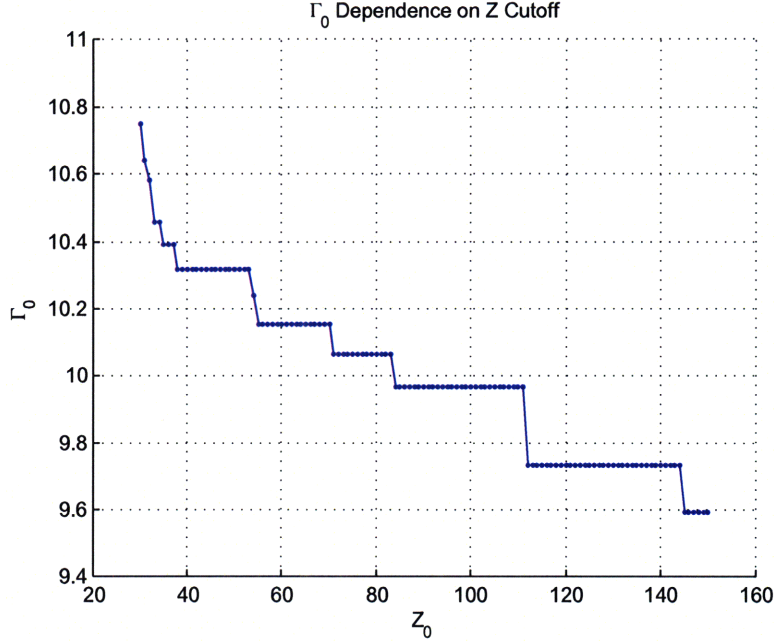


Figure 4-7: The dependence of the Γ threshold on the Z^{Coh} threshold for year 2. The relationship between Γ_0 and Z_0^{Coh} is determined by setting a false alarm probability of 1/100.

4.5.3 Final Plan for Year 2 Analysis

The final plan for the analysis of the year 2 foreground data is the same as that for year 1, but with a different Z^{Coh} threshold:

- $Z_0^{Coh} = 75$
- $\Gamma_0 = 10.1$

Figure 4-9 shows the efficiencies for the year 2 analysis, compared to the efficiencies for the year 1 analysis. Because of the improvements made to LIGO in the first few months of year 1, the year 2 analysis is slightly more sensitive.

4.6 Test of the Analysis on Timelagged Data

Before applying the analysis to the foreground data, the background data were compared to timelagged data as a check on the background Γ distribution. Two timeslides

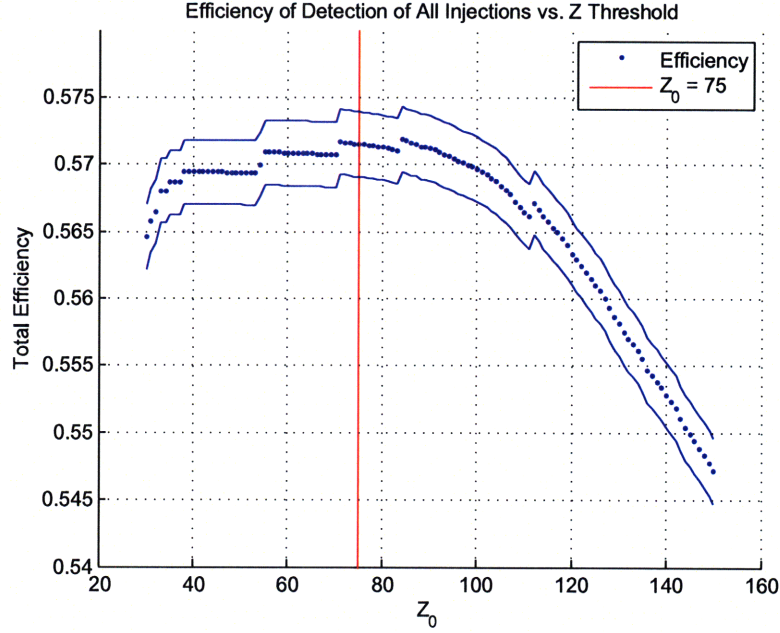


Figure 4-8: The efficiency of detection of all types of injections in year 2 background data for a range of Z_{Coh} thresholds. The blue lines indicate the error on the efficiency. The red line marks $Z_0^{Coh} = 75$, which would be at the maximum efficiency if the efficiency curve was smooth.

were created by shifting the foreground data from H1 relative to H2 by 5 seconds and 10 seconds. Since this analysis is searching for gravitational-wave bursts that have a duration of much less than a second, and the light travel time between the two Hanford detectors is on the order of 10 ms, the timelagged data should simulate noise in the absence of gravitational waves.

For each of the two timeslides, the data were analyzed using the finalized methods for year 1 and year 2 described in sections 4.4.5 and 4.5.3. The Γ distribution of the timelagged data agreed well with the Γ distribution of the triple-coincident data for both years, confirming that the false alarm probability of 1% is reasonable. Figure 4-10 compares the Γ distributions of the timelagged data and the background data for year 1, and figure 4-11 shows the same comparison for year 2; in these figures the distributions from the two timelags are added together, so the livetime of the timelagged distribution is approximately twice the foreground livetime.

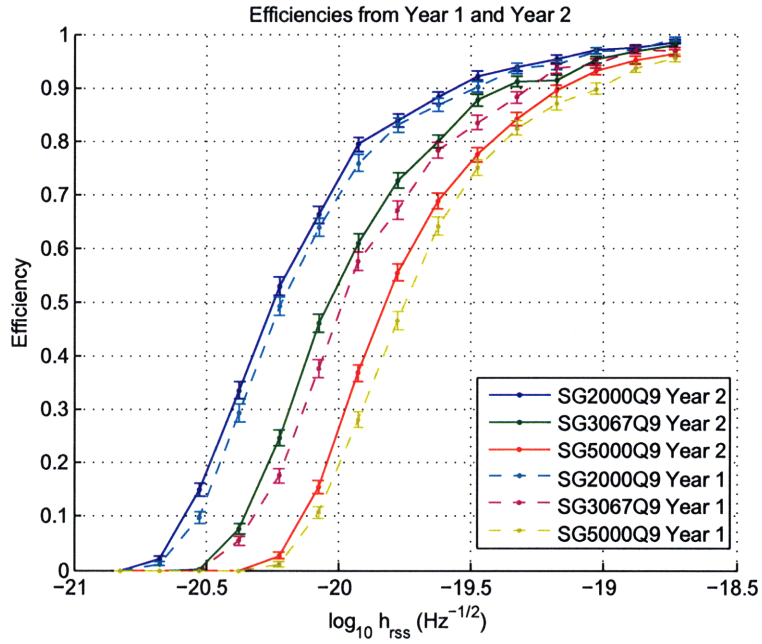


Figure 4-9: The final efficiency of detection of injections for year 2 (solid lines), compared to year 1 (dashed lines). Year 2 is slightly more efficient than year 1 because of improvements made to the detectors partway through year 1.

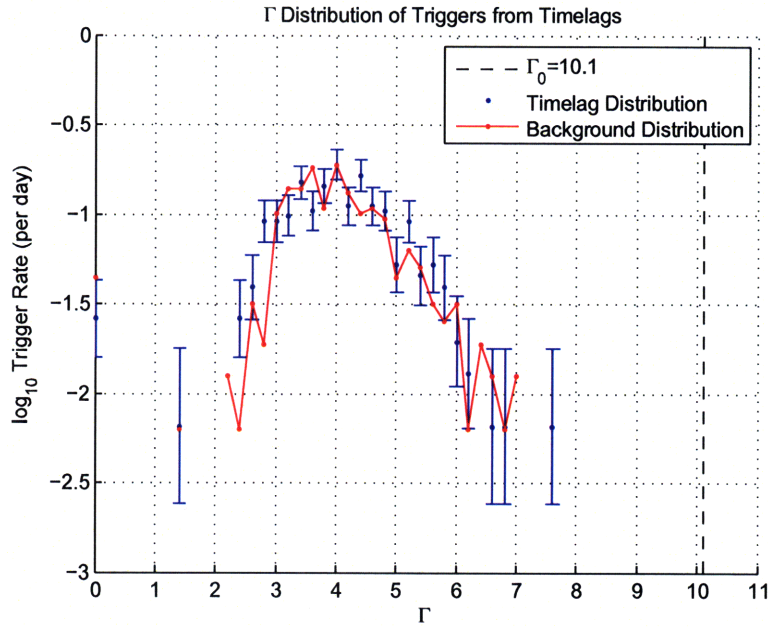


Figure 4-10: The Γ distribution of triggers from year 1 timelagged data that passed the normalized energy threshold $Z^{Coh} = 100$, compared to the background distribution. The timelagged data are a combination of two time slides of 5 seconds and 10 seconds. The distributions are normalized relative to their respective livetimes. To keep the plot legible, error bars are not shown on the background distribution, but are of approximately the same size as for the foreground distribution. The Γ threshold of 10.1 is shown on the right of the plot for reference.

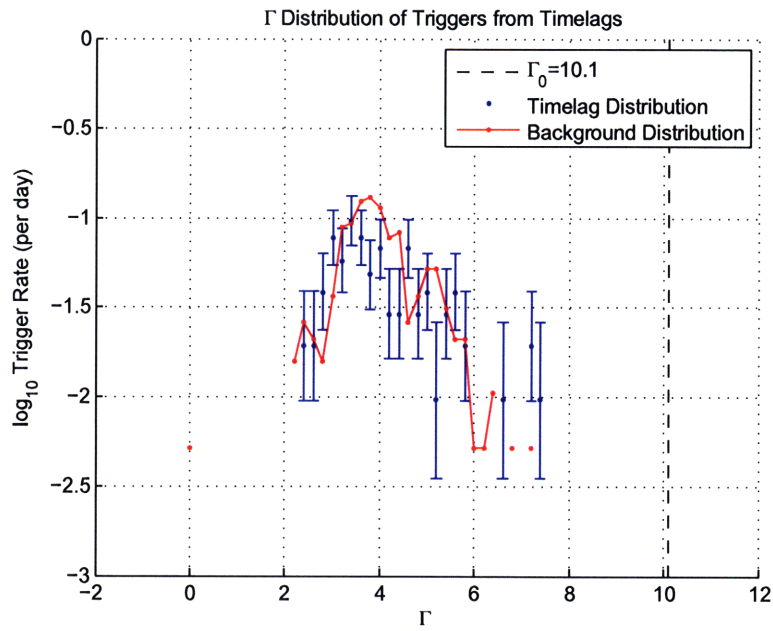


Figure 4-11: The Γ distribution of triggers from year 2 timelagged data that passed the normalized energy threshold $Z^{Coh} = 75$, compared to the background distribution. The distributions are normalized relative to their respective livetimes. Error bars are not shown on the background distribution, but are of approximately the same size as for the foreground distribution.

Chapter 5

Results and Discussion

After the design of each year's analysis was completed, the foreground data were analyzed. The foreground data from year 1 were analyzed before the year 2 analysis was started. In both years, no triggers passed both the coherent energy and Γ thresholds, so there were no gravitational-wave candidates. Poisson statistics were used to set an upper limit on the rate of high-frequency gravitational-wave bursts.

5.1 Γ Distribution of Triggers

The Γ distribution of triggers that passed the coherent energy threshold are shown in Figures 5-1 and 5-2. As mentioned in Chapter 4, the vetoes were not applied during the training of the analysis, so the Γ distributions in Figures 5-1 and 5-2 are shown before the vetoes were applied. When the vetoes were applied, they cut out about half of the triggers that passed the normalized energy cut.

The Γ distributions of the background and the foreground in each year are consistent to within the errors. In year 1 there was a higher rate of foreground triggers with high Γ than background triggers. These high- Γ foreground triggers were examined in further detail, as described in Section 5.1.1.

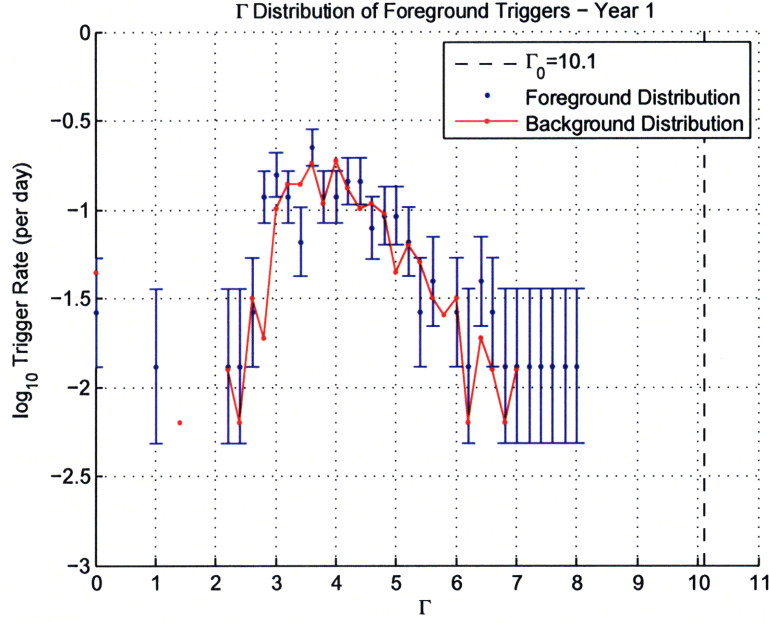


Figure 5-1: Γ distribution of triggers from the year 1 foreground that passed the coherent energy threshold $Z_0^{Coh} = 100$, compared to the Γ distribution of the background triggers. The distributions are normalized to livetime. No triggers passed the Γ threshold of 10.1, shown by a dotted black line. The error bars on the background are not shown but are similar in size to the errors on the foreground.

5.1.1 Inspection of High- Γ Triggers

The highest- Γ triggers from each year's foreground were examined using QScan, software that plots the Q transform of an individual burst and of auxiliary channels at the time of the burst. For completeness, the three highest- Γ triggers from year 2 were also examined using QScan. For all of these triggers, the glitch was much larger in H1 than in H2, suggesting that it was artificial in origin. Had the null stream veto been applied, it would have eliminated these triggers. Figure 5-3 shows the Q transform of the H1 and H2 main channels for the highest- Γ trigger from year 1 that was not vetoed.

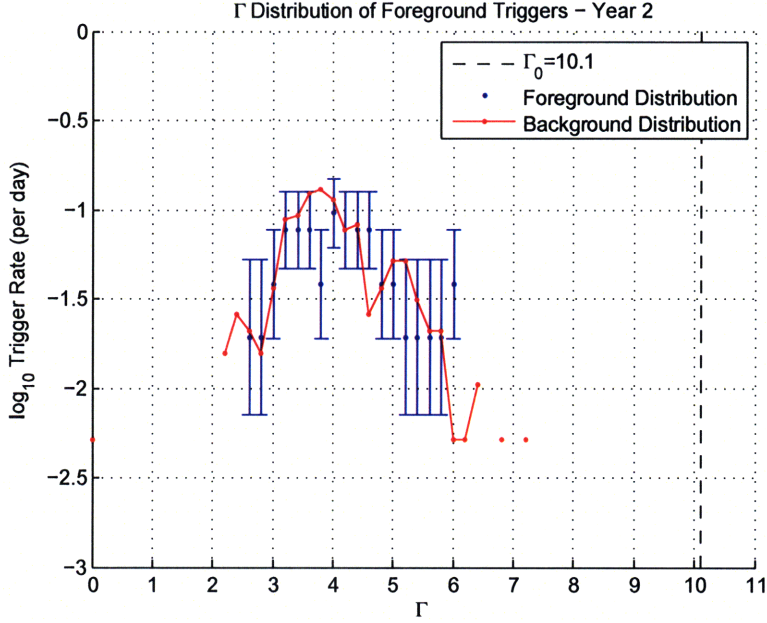


Figure 5-2: Γ distribution of triggers from the year 2 foreground that passed the coherent energy threshold $Z_0^{Coh} = 75$, compared to the Γ distribution of the background triggers. The distributions are normalized to livetime. No triggers passed the Γ threshold of 10.1. The error bars on the background, though not shown, are about half the size of the error bars on the foreground.

5.2 Upper Limit Curves

The result of no detections placed an upper limit on the rate of gravitational waves reaching Earth. A standalone MATLAB code was used to make an analytical fit to the efficiency curves for the injections, and from these efficiencies upper limits were calculated for each amplitude and frequency of sine-Gaussian burst.

Given no events above threshold, Poisson statistics set an upper limit on the average rate of gravitational-wave events at 2.3 events per livetime, with 90% confidence. This upper limit is the rate for which the Poisson probability of observing zero events during the livetime of the experiment is 90% [12].

Dividing the upper limit of 2.3 events per livetime by the livetime in days yields the upper limit on number of gravitational-wave detections per day for 100% efficiency. Dividing by the efficiency of detection $\text{Eff}(h_{rss}, f_0)$ for a certain h_{rss} and central frequency f_0 converts to the upper limit $\text{UL}(h_{rss}, f_0)$ on the rate of gravitational waves

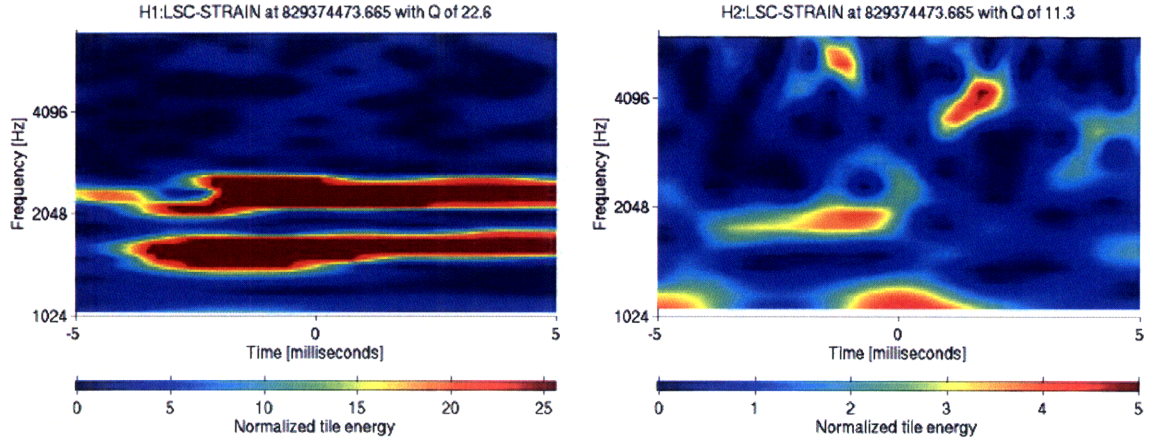


Figure 5-3: Q transform of the H1 and H2 main channels. The two plots are scaled differently because the burst is significantly larger in H1 than in H2. The highest- Γ triggers in both years' foregrounds had large bursts in H1 and much smaller bursts in H2, which would not occur for true gravitational waves.

of that h_{rss} and frequency.

$$\text{UL}(h_{rss}, f_0) = \frac{2.3 \text{ events}}{\text{lifetime} * \text{efficiency}(h_{rss}, f_0)}. \quad (5.1)$$

Figure 5-4 shows the upper limit curves from the year 1 and year 2 analyses, for a range of frequencies and amplitudes. As shown in Figure 4-9, the year 2 analysis had higher efficiencies for detecting gravitational waves, but the year 2 foreground livetime was 30% shorter than the year 1 foreground, so the year 1 analysis set a stronger upper limit on the rate of high-frequency gravitational-wave bursts passing through Earth. As h_{rss} increases, the upper limits for the three frequencies converge, corresponding to the point where the efficiency of the analysis approaches 1 for all three frequencies. The year 1 upper limits converge to a slightly lower rate than for year 2, because of year 1's longer foreground livetime.

The upper limits from the two years were combined by weighting each year's efficiencies according to that year's livetime. Figure 5-5 shows the combined upper limit curves. Since there was no detection in either year, with 100% efficiency above $h_{rss} = 10^{-19}$ strain/ $\sqrt{\text{Hz}}$, the upper limit for gravitational waves of such an amplitude is 2.3 divided by the foreground livetime of the two analyses combined, a total of 130.1

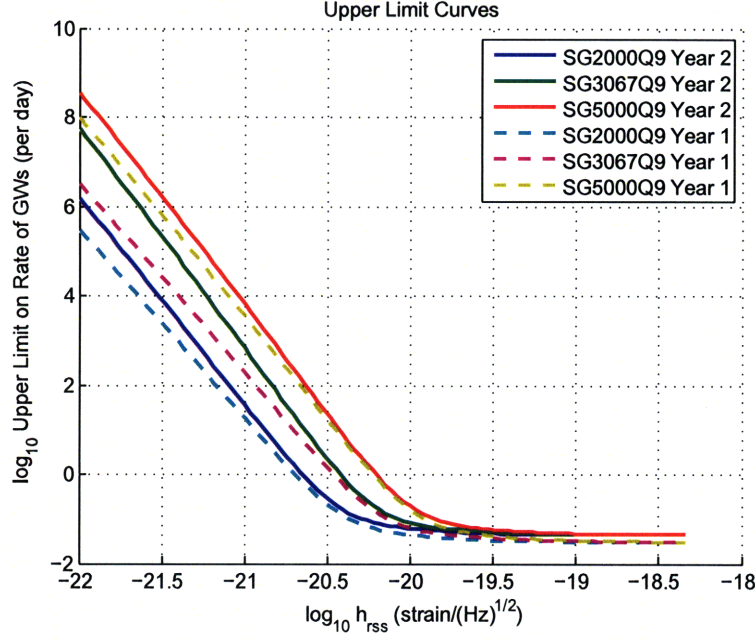


Figure 5-4: Upper limits from each year’s analysis on the rate of gravitational-wave bursts of varying frequency and amplitude. The upper limits set by the year 1 analysis are shown with dotted lines; year 2, with solid lines. Systematic error on h_{rss} is on the order of 10%. The year 1 analysis set slightly better limits than the year 2 analysis because of year 1’s longer foreground livetime. The year 1 upper limits for all frequencies converge of a limit of one gravitational wave every 74 days for h_{rss} values greater than 10^{-19} strain/ \sqrt{Hz} .

days. This upper limit is 0.018 gravitational waves per day, or 6.5 per year.

5.3 Potential Improvements to the Analysis

Future similar analyses may be improved by avoiding challenges faced by this analysis. Conducting a blind analysis means that once the foreground data has been analyzed, if a minor error in the design of the analysis is found, it is undesirable to go back and change the analysis, as it may introduce bias. This analysis made the minor error of failing to apply the vetoes during the analysis design before analyzing the foreground data.

Furthermore, this analysis was limited by the timing: a final calibration for S5 was not yet available when the box was opened on the year 1 data. The provisional

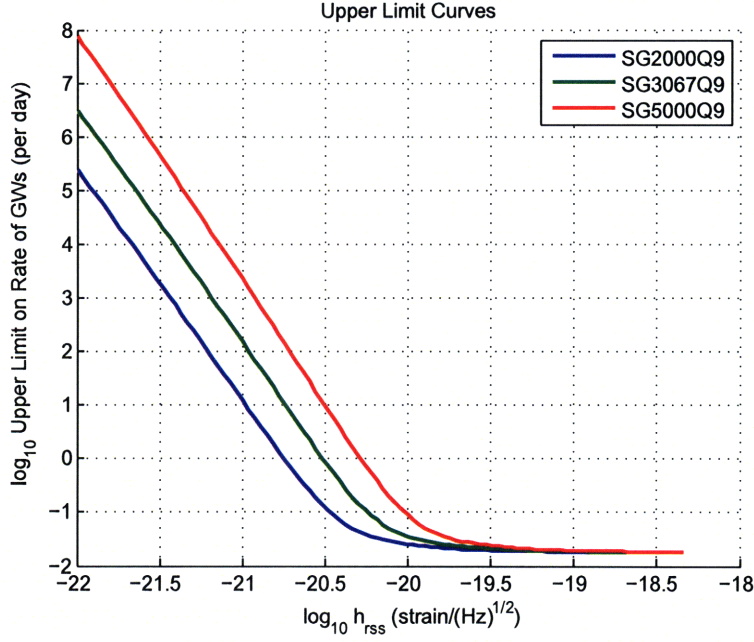


Figure 5-5: Combined upper limits on the rate of gravitational-wave bursts of varying frequency and amplitude. To combine the upper limits from year 1 and year 2, their livetimes are weighted by their efficiencies. Systematic error on h_{rss} is on the order of 10%. The upper limits for all frequencies converge to a limit of one gravitational wave every 55 days for h_{rss} values greater than 10^{-19} strain/ $\sqrt{\text{Hz}}$.

calibration used had larger phase shifts at high frequencies than the final calibration, so the negative effect of applying the null stream veto was overestimated. Future analyses should not rule out the option of applying the null stream veto, which may lead to a slight improvement in efficiency. Another possible way to improve efficiency would be to run QPipeline on the H1 and H2 main channels separately, and then cut out triggers with too large a difference between coherent energy in H1 and coherent energy in H2. This cut would not be sensitive to phase shift, unlike the null stream veto. The highest- Γ triggers, inspected using QScan, all had large bursts in H1 and relatively small fluctuations in H2; this cut would remove such triggers, but not real gravitational-wave signals, improving the sensitivity of the analysis.

5.4 Context

This analysis was conducted using a double-coincidence requirement for data from LIGO's fifth science run, during which LIGO was at its design sensitivity. This thesis contributed to LIGO's high-frequency burst search for year 1 of S5 [7], the first search for gravitational-wave bursts ever to cover all frequencies from 1 to 6 kHz, which set an unprecedented upper limit of 0.014 high-frequency gravitational waves per day at a 90% confidence level.

Beyond the LIGO detectors, Virgo has started collecting data, and so future analyses may use a quadruple-coincidence requirement, significantly improving the ability to detect gravitational waves. In addition, Advanced LIGO is planned to be introduced by 2014; Advanced LIGO is anticipated to improve on the sensitivity of LIGO by an order of magnitude [19]. Finally, the chances of detecting gravitational waves are also being furthered by collaboration to correlate data from gravitational-wave interferometers to astronomical data collected through electromagnetic observations [26].

Bibliography

- [1] B. Abbott et al. LIGO: The Laser Interferometer Gravitational-Wave Observatory. 2007. Available online at <http://arxiv.org/abs/0711.3041>.
- [2] B. Abbott et al. Search for gravitational-wave bursts in LIGO data from the fourth science run. *Class. Quant. Grav.*, 24:5343–5370, 2007.
- [3] B. Abbott et al. Searching for a stochastic background of gravitational waves with LIGO. *Astrophys. J.*, 659:918–930, 2007.
- [4] B. Abbott et al. All-sky LIGO search for periodic gravitational waves in the early S5 data. *Physical Review Letters*, 102:111102, 2009.
- [5] B. Abbott et al. Search for gravitational-wave bursts in the first year of the fifth LIGO science run. 2009. Submitted for publication. Available online at <http://arxiv.org/abs/0905.0020>.
- [6] B. Abbott et al. Search for Gravitational Waves from Low Mass Binary Coalescences in the First Year of LIGO’s S5 Data. 2009. Submitted for publication. Available online at <http://arxiv.org/abs/0901.0302>.
- [7] B. Abbott et al. Search for high frequency gravitational wave bursts in the first calendar year of LIGO’s fifth science run. 2009. Submitted for publication. Available online at <http://arxiv.org/abs/0904.4910>.
- [8] A. Abramovici et al. LIGO: The Laser Interferometer Gravitational-Wave Observatory. *Science*, 256(5055):325–333, 1992.
- [9] W. G. Anderson et al. Excess power statistic for detection of burst sources of gravitational radiation. *Phys. Rev. D*, 63(4):042003–+, February 2001.
- [10] L. Baiotti et al. On the gravitational radiation from the collapse of neutron stars to rotating black holes. *Classical and Quantum Gravity*, 24:187–+, June 2007.
- [11] L. Baiotti and L. Rezzolla. Challenging the Paradigm of Singularity Excision in Gravitational Collapse. *Physical Review Letters*, 97(14):141101–+, October 2006.
- [12] P. R. Brady et al. Upper limits on gravitational-wave signals based on loudest events. *Classical and Quantum Gravity*, 21:1775–+, October 2004.

- [13] M. Burgay et al. An increased estimate of the merger rate of double neutron stars from observations of a highly relativistic system. *Nature*, 426:531–533, December 2003.
- [14] L. Cadonati and S. Márka. CorrPower: a cross-correlation-based algorithm for triggered and untriggered gravitational-wave burst searches. *Classical and Quantum Gravity*, 22:1159–+, September 2005.
- [15] Fabien Cavalier. Gravitational waves in general relativity. <http://publication.lal.in2p3.fr/2001/web/node3.html>.
- [16] I. Chakrabarty. Gravitational waves: An introduction. 1999. Available online at <http://arxiv.org/abs/physics/9908041v1>.
- [17] S. Chatterji et al. Multiresolution techniques for the detection of gravitational-wave bursts. *Classical and Quantum Gravity*, 21:1809–+, October 2004.
- [18] Shourov Chatterji. *The search for gravitational-wave bursts in data from the second LIGO science run*. PhD dissertation, MIT, Department of Physics, 2005.
- [19] P. Fritschel. Second generation instruments for the Laser Interferometer Gravitational Wave Observatory (LIGO). In M. Cruise and P. Saulson, editors, *Society of Photo-Optical Instrumentation Engineers (SPIE) Conference Series*, volume 4856, pages 282–291, March 2003.
- [20] GEO600. <http://www.geo600.uni-hannover.de/>.
- [21] M. E. Gertsenshtein and V. I. Pustovoit. On the detection of low-frequency gravitational waves. *Sov. Phys. JETP*, 16:433, 1962.
- [22] J. E. Horvath. Energetics of the Superflare from SGR1806-20 and a Possible Associated Gravitational Wave Burst. *Modern Physics Letters A*, 20:2799–2804, 2005.
- [23] R. A. Hulse and J. H. Taylor. Discovery of a pulsar in a binary system. *Ap. J.*, 195:L51–L53, January 1975.
- [24] K. T. Inoue and T. Tanaka. Gravitational Waves from Sub-Lunar-Mass Primordial Black-Hole Binaries: A New Probe of Extradimensions. *Physical Review Letters*, 91(2):021101–+, July 2003.
- [25] J. G. Jernigan. KiloHertz QPO and Gravitational Wave Emission as the Signature of the Rotation and Precession of a LMXB Neutron Star Near Breakup. In J. C. Wheeler and H. Martel, editors, *20th Texas Symposium on relativistic astrophysics*, volume 586 of *American Institute of Physics Conference Series*, pages 805–+, 2001.
- [26] J. Kanner et al. LOOC UP: locating and observing optical counterparts to gravitational wave bursts. *Classical and Quantum Gravity*, 25(18):184034–+, September 2008.

- [27] LIGO. <http://www.ligo.caltech.edu/>.
- [28] LIGO-Caltech. http://www.ligo.caltech.edu/LIGO_web/PR/scripts/facts.html.
- [29] H. J. Mosquera Cuesta and D. M. González. Bursts of gravitational radiation from superconducting cosmic strings and the neutrino mass spectrum. *Physics Letters B*, 500:215–221, February 2001.
- [30] G. E. Moss, L. R. Miller, and R. L. Forward. Photon-noise-limited laser transducer for gravitational antenna. *Appl. Opt.*, 10:2495–2498, 1971.
- [31] R. Oechslin and H.-T. Janka. Gravitational Waves from Relativistic Neutron-Star Mergers with Microphysical Equations of State. *Physical Review Letters*, 99(12):121102–+, September 2007.
- [32] C. D. Ott et al. Gravitational Waves from Axisymmetric, Rotating Stellar Core Collapse. *Ap. J.*, 600:834–864, January 2004.
- [33] T. A. Prince et al. Timing observations of the 8 hour binary pulsar 2127 + 11C in the globular cluster M15. *Ap. J.*, 374:L41–L44, June 1991.
- [34] P.R. Saulson. *Fundamentals of Interferometric Gravitational Wave Detectors*. World Scientific, Singapore; River Edge, U.S.A., 1994.
- [35] B. F. Schutz. Gravitational wave astronomy. *Classical and Quantum Gravity*, 16:A131–A156, December 1999.
- [36] S. Shourov. The fast discrete Q-transform, November 2003. LIGO Document LIGO-G030544-00-Z. Available online at <http://www.ligo.caltech.edu/docs/G/G030544-00.pdf>.
- [37] I. H. Stairs et al. Studies of the Relativistic Binary Pulsar PSR B1534+12. I. Timing Analysis. *Ap. J.*, 581:501–508, December 2002.
- [38] A. L. Stuver and L. S. Finn. GravEn: software for the simulation of gravitational wave detector network response. *Classical and Quantum Gravity*, 23:799–+, October 2006.
- [39] TAMA. <http://tamago.mtk.nao.ac.jp/>.
- [40] K. S. Thorne. Multipole expansions of gravitational radiation. *Reviews of Modern Physics*, 52:299–340, April 1980.
- [41] Virgo. <http://www.virgo.infn.it/>.
- [42] J. Weber. Detection and generation of gravitational waves. *Phys. Rev.*, 117(1):306–313, Jan 1960.
- [43] J. M. Weisberg and J. H. Taylor. The Relativistic Binary Pulsar B1913+16. In M. Bailes, D. J. Nice, and S. E. Thorsett, editors, *Radio Pulsars*, volume 302 of *Astronomical Society of the Pacific Conference Series*, pages 93–+, 2003.

- [44] Rainer Weiss. Electromagnetically coupled broadband gravitational antenna. *Quarterly Progress Report of the Research Laboratory of Electronics*, 105:54, April 1972.